


Article

Mechanical and Tribological Properties of (AlCrNbSiTiMo)N High-Entropy Alloy Films Prepared Using Single Multiple-Element Powder Hot-Pressed Sintered Target and Their Practical Application in Nickel-Based Alloy Milling

Jeng-Haur Horng^{1,2} , Wen-Hsien Kao^{3,*}, Wei-Chen Lin⁴ and Ren-Hao Chang⁴

¹ Department of Power Mechanical Engineering, National Formosa University, Yunlin 632, Taiwan; jhhorng@gmail.com

² International Master's Program in Interdisciplinary Sustainability Studies, National Cheng Kung University, Tainan 701, Taiwan

³ Department of Mechanical Engineering, Institute of Manufacturing Technology, Chienkuo Technology University, Changhua 500, Taiwan

⁴ Department of Mechanical Engineering, National Cheng Kung University, Tainan 701, Taiwan; n16111552@gs.ncku.edu.tw (W.-C.L.); n16124987@gs.ncku.edu.tw (R.-H.C.)

* Correspondence: n18851158@yahoo.com.tw; Tel.: +886-4-7111111 (ext. 2414)

Abstract: (AlCrNbSiTiMo)N high-entropy alloy films with different nitrogen contents were deposited on tungsten carbide substrates using a radio-frequency magnetron sputtering system. Two different types of targets were used in the sputtering process: a hot-pressing sintered AlCrNbSiTi target fabricated using a single powder containing multiple elements and a vacuum arc melting Mo target. The deposited films were denoted as R_{N0} , R_{N33} , R_{N43} , R_{N50} , and R_{N56} , where R_N indicates the nitrogen flow ratio relative to the total nitrogen and argon flow rate ($R_N = (N_2 / (N_2 + Ar)) \times 100\%$). The as-sputtered films were vacuum annealed, with the resulting films denoted as HR_{N0} , HR_{N33} , HR_{N43} , HR_{N50} , and HR_{N56} , respectively. The effects of the nitrogen content on the composition, microstructure, mechanical properties, and tribological properties of the films, in both as-sputtered and annealed states, underwent thorough analysis. The R_{N0} and R_{N33} films displayed non-crystalline structures. However, with an increase in nitrogen content, the R_{N43} , R_{N50} , and R_{N56} films transitioned to FCC structures. Among the as-deposited films, the R_{N43} film exhibited the best mechanical and tribological properties. All of the annealed films, except for the HR_{N0} film, displayed an FCC structure. In addition, they all formed an MoO_3 solid lubricating phase, which reduced the coefficient of friction and improved the anti-wear performance. The heat treatment HR_{N43} film displayed the supreme hardness, H/E ratio, and adhesion strength. It also demonstrated excellent thermal stability and the best wear resistance. As a result, in milling tests on Inconel 718, the R_{N43} -coated tool demonstrated a significantly lower flank wear and notch wear, indicating an improved machining performance and extended tool life. Thus, the application of the R_{N43} film in aerospace manufacturing can effectively reduce the tool replacement cost.

Keywords: high entropy alloy; single multiple-element powder; tribological properties; thermal stability; machining performance



Citation: Horng, J.-H.; Kao, W.-H.; Lin, W.-C.; Chang, R.-H. Mechanical and Tribological Properties of (AlCrNbSiTiMo)N High-Entropy Alloy Films Prepared Using Single Multiple-Element Powder Hot-Pressed Sintered Target and Their Practical Application in Nickel-Based Alloy Milling. *Lubricants* **2024**, *12*, 391. <https://doi.org/10.3390/lubricants12110391>

Received: 16 October 2024

Revised: 6 November 2024

Accepted: 12 November 2024

Published: 14 November 2024



Copyright: © 2024 by the authors. Licensee MDPI, Basel, Switzerland. This article is an open access article distributed under the terms and conditions of the Creative Commons Attribution (CC BY) license (<https://creativecommons.org/licenses/by/4.0/>).

1. Introduction

As industrial technologies continue to advance, the demand for improved mechanical properties and superior processing of components and materials has steadily increased. For example, the Ni-based alloys currently utilized in the aerospace applications possess excessively high hardness and are therefore difficult to machine. Consequently, the traditional films used to enhance the machining performance and service life of cutting tools are no longer adequate. Therefore, there is a pressing need for new films with superior

mechanical, tribological, and thermal stability properties to satisfy the demands of modern processing environments.

In 2002, Cantor et al. [1] proposed a new class of alloys, referred to as multi-principal element alloys (MPEAs), composed of multiple elements, each with a concentration between 5 and 35% (at.% or wt.%) [1]. The underlying aim of MPEAs is to tailor the properties of the alloy through a careful selection of the constitutive elements and their relative proportions. In 2004, Yeh et al. [2] refined the concept of MPEAs by introducing high-entropy alloys (HEAs), in which the properties of the alloy were enhanced by deliberately inducing high configurational entropy in the alloy system, rather than simply exploiting the synergistic effects of the individual elements. HEAs exhibit four primary characteristics: (1) high entropy, (2) slow diffusion, (3) lattice distortion, and (4) cocktail [3]. Collectively, these characteristics provide HEA films with excellent performance, including high hardness [4], superior wear resistance [5], enhanced corrosion resistance [6], and good thermal stability [3].

The literature contains extensive studies on many HEAs, including (CrTaNbMoV)N [7], (AlCrMoSiTi)N [8], (CrAlNbSiV)N [9], and (AlCrNbSiTiV)N [3,10]. These films show excellent mechanical properties [3,8,9], outstanding wear resistance [7,9], superior high-temperature stability [3], and a good machining performance in general cutting processes [10]. Nonetheless, there is still a requirement for HEA films capable of meeting the challenging demands of machining applications involving high-hardness alloys, such as nickel-based alloys. The oxidation resistance temperatures of traditional films for instance TiAlN, TiN, and diamond-like carbon (DLC) are 800 °C [11], 600 °C [11], and 350 °C [12], respectively. These temperatures are much lower than those generated during the processing of nickel-based alloys such as Inconel 718 (950 °C) [13]. Thus, these films suffer extensive damage during cutting, which greatly reduces their processing performance and increases the tool replacement cost.

To address this issue, the present study proposes a novel six-element HEA consisting of aluminum (Al), silicon (Si), titanium (Ti), chromium (Cr), niobium (Nb), and molybdenum (Mo). The addition of Al and Cr to the alloy system promotes the formation of Al₂O₃ and Cr₂O₃ phases, which improve the oxidation resistance of the film [14–16]. Meanwhile, the Nb and Ti contents improve the hardness of the film [17,18], while the Si and Mo enhance the wear resistance [19,20]. Molybdenum forms MoO₃ solid lubricant in high-temperature environments [21], thereby reducing the coefficient of friction (COF) and enhancing the wear performance. Moreover, the addition of Mo to the alloy system also prompts a solid-solution strengthening effect, which improves the hardness and thermal stability of the film [22].

Previous studies have shown that films prepared using AlCrNbSiTi targets produced by arc melting followed by traditional powder hot-pressing sintering possess good mechanical properties and excellent wear resistance [23–25]. Building on these findings, the mechanical and tribological properties of the proposed AlCrNbSiTiMo film are further enhanced by performing the sputtering process using a single high-purity Mo target, a Cr target, and two AlCrNbSiTi targets fabricated by the hot-press sintering of a single multiple-element powder containing Al, Cr, Nb, Si, and Ti. The films are sputtered with various nitrogen flow rates. The film with the optimal mechanical and tribological properties is selected for milling trials on Inconel 718. It is shown that the selected film results in a decreased notch wear and flank wear than previous six-element HEA films under identical machining conditions. It thus appears to be promising for the processing of aerospace difficult-to-machine materials, with the potential to increase the tool life and reduce the tool replacement cost.

2. Materials and Methods

2.1. Preparation of Target Materials and Films

(AlCrNbSiTiMo)N films were deposited on Si, WC substrates, and WC cutting tools. Detailed substrate specifications and sputtering equipment are provided in [26]. The system utilized four targets, each with dimensions of 300 mm × 109 mm × 10 mm (Figure 1a). As

shown in Figure 1b, the film comprised Cr as the interlayer, CrN as the gradient layer, and a final main film layer of AlCrNbSiTiMo+N, deposited by sputtering. The Si substrate was used to observe the cross-sectional structure and thickness of the as-deposited films. The WC disk was used to evaluate the adhesion strength, hardness, and wear resistance of the films under both as-deposited and annealed conditions.

The Mo and Cr targets were fabricated using vacuum arc melting and had purities greater than 99.99%. The multi-element targets used for the deposition of HEA films are generally fabricated via hot-press sintering or arc melting [3,10,23–25]. In such methods, metallic powders are mixed through ball milling or atomization and then sintered under high pressure or fused via vacuum arc melting. By contrast, in the present study, the AlCrNbSiTi targets were fabricated by fusing the various metallic elements and then grinding the resulting material into particles. In other words, the hot-pressing sintering process was performed using a single powder containing multiple elements (Al, Cr, Nb, Si, and Ti) rather than multiple powders each containing a single element. The films prepared in this manner were expected to achieve a denser film structure, higher hardness, and better wear resistance.

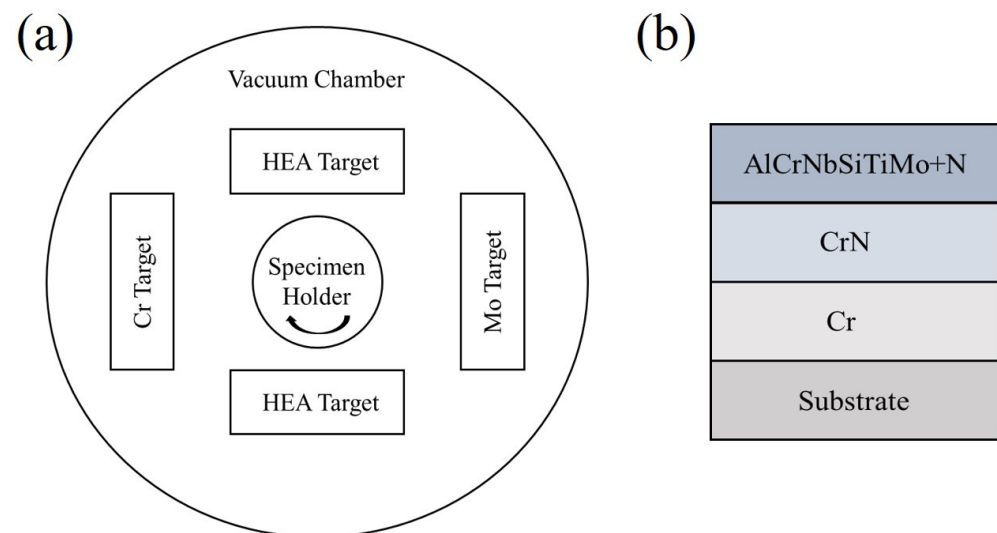
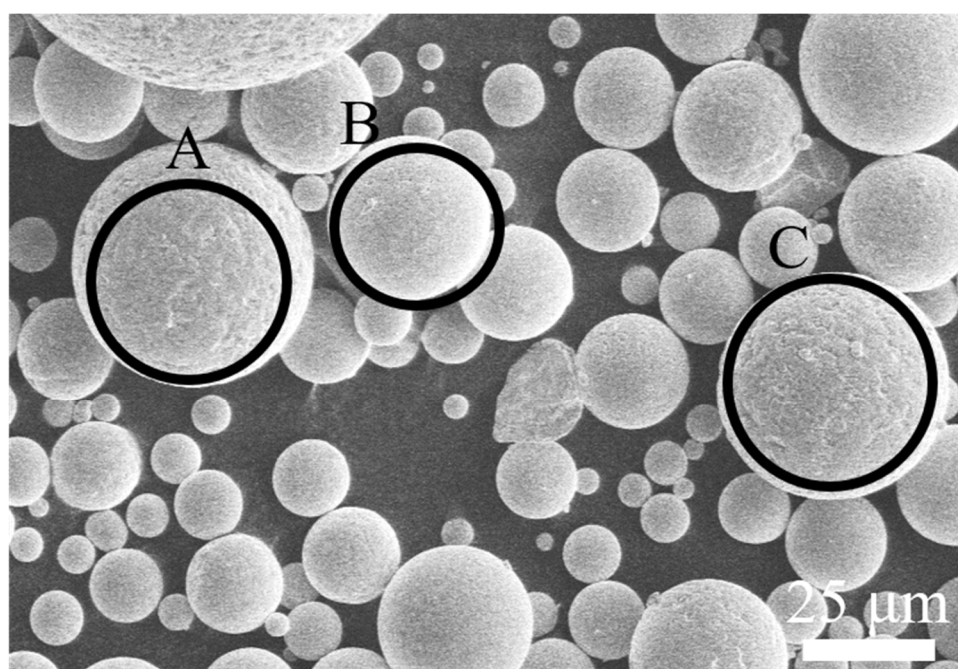


Figure 1. (a) Diagrammatic sketch of sputtering target configuration, and (b) diagrammatic sketch of film design.

As shown in Figure 2, the powder particles had different sizes but contained all the target elements. The standard deviation of the compositions of the five elements in the different particles was just $\pm 0.1 \sim \pm 0.5\%$. In other words, the multiple-element powder contained a uniform composition of the different elements. The particle size distribution of metallic powders is commonly characterized using length values of D_{10} , D_{50} , and D_{90} (μm), where D_{10} indicates that 10% of the powder particles in the cumulative distribution possess a diameter smaller than or equal to the corresponding value, D_{50} signifies that 50% of the powder particles have diameters smaller than or equal to the corresponding value, and D_{90} indicates that 90% of the powder particles have diameters smaller than or equal to the corresponding value [27]. For the present AlCrNbSiTi powder, the D_{10} , D_{50} , and D_{90} values were 20.87, 69.42, and 157.66 μm , respectively.



at.%	A	B	C	SD
Al	32.9	33.4	32.3	±0.5
Cr	22.7	22.4	23.0	±0.3
Nb	11.0	10.9	11.0	±0.1
Si	11.3	11.2	11.3	±0.1
Ti	22.2	22.1	22.4	±0.1

Figure 2. Morphology and elemental composition of new AlCrNbSiTi powder for hot-pressing sintering targets.

The targets and substrate pre-treated by sputtering with Argon ions at a flux of 20 sccm for 10 min to remove surface contaminants. The sputtering process was performed with a chamber base pressure of 2.67×10^{-3} Pa, and the specimen was rotated continuously at 2 rpm to ensure a uniform distribution of the film on the substrate. To improve the adhesion between the main film and the substrate, the deposition process was divided into three stages: interlayer deposition, transitional layer deposition, and main film layer deposition. The interlayer was deposited using a constant Ar flow rate of 20 sccm, a bias voltage of -150 V, a Cr target current of 1.5 A, and a deposition time of 20 min. The transitional layer was prepared using a bias voltage of -50 V, nitrogen (N) flow rate of 8 sccm, and deposition time of 15 min. Finally, the main film was deposited using a bias voltage of -50 V, AlCrNbSiTi and Mo target currents of 1.5 A, a deposition time of 80 min, and N gas flux rates of 0 to 25 sccm were used, and for simplicity, the resulting films were labeled as R_{N0} , R_{N33} , R_{N43} , R_{N50} , and R_{N56} , respectively, where R_N indicates the ratio of the N flow rate to the total (N and Ar) flow rate ($R_N = (N_2/N_2+Ar) \times 100\%$). Detailed deposition parameters are listed in Table 1.

Table 1. Deposition parameters for each film.

Variable Parameters		Constant Parameters		
Film Name	Nitrogen Flux (sccm)	Interlayer (Cr)	Transitional Layer (CrN)	Main Film (AlCrNbSiTiMo)
R _{N0}	0	Deposition time: 20 min	Deposition time: 15 min	Deposition time: 80 min
R _{N33}	10	Cr Target set current: 1.5 A	Cr Target current: 1.5 A	AlCrNbSiTi target set current: 1.5 A
R _{N43}	15	Argon flow rate: 20 sccm	Nitrogen flux: 8 sccm	Mo target set current: 1.5 A
R _{N50}	20	Substrate bias: −150 V	Argon flow rate: 20 sccm	Argon flow rate: 20 sccm
R _{N56}	25		Substrate bias: −150 V	Substrate bias: −50 V

Following the deposition process, the R_{N0}, R_{N33}, R_{N43}, R_{N50}, and R_{N56} films were vacuum-annealed. The heat-treatment process is described in detail in [26]. For convenience, the heat-treatment films were named as HR_{N0}, HR_{N33}, HR_{N43}, HR_{N50}, and HR_{N56}, respectively.

2.2. Characterization, Mechanical Properties, and Adhesion Strength

The elemental contents of the films were analyzed by energy-dispersive spectrometry (EDS). The crystal structures were examined using X-ray diffraction (XRD). The chemical compositions of the films were determined using X-ray photoelectron spectroscopy (XPS). The structures were examined using scanning electron microscopy (SEM). The surface roughness was measured using a white-light interferometer (WLI). The hardness and Young's modulus were assessed by a nanoindentation tester. To prevent substrate effects, the highest indentation depth was kept to under one-tenth the film thickness [28,29]. The adhesion strengths of the annealed films were assessed using a scratch tester fitted with a spherical diamond indenter with a diameter of 0.3 mm. The adhesion strength was determined as the load when the film first exhibited continuous peeling from the substrate. The details and setups of the measurement instruments are presented in [26].

2.3. Tribological Characteristics

The tribological behavior of the films were determined utilizing a ball-on-disk testing system. The detailed equipments are provided in [26]. The sliding wear tests used a Grade 5 Si₃N₄ sphere (Ø2.38 mm) as the counterbody. The ball had a composition of 24.62 at.% Si and 75.38 at.% N. The maximum surface roughness was Ra = 0.014 µm, and the hardness was 80 HRC. The test environment was established in accordance with the ASTM G99 [30] standard, with a temperature of 25 °C, a relative humidity of 50%, 0 sccm of argon gas, and no lubricant added. The COF was continuously documented during the test. Following the tests, the wear area and wear depth for every wear pair were measured using the WLI. The detailed parameter of experimental setup and worn rate calculation are provided in [26]. The wear surface was analyzed using SEM, and the elemental composition was assessed using EDS.

2.4. Milling Performance

Milling tests were performed on a five-axis CNC milling machine using Inconel 718 materials. The detailed elemental composition and dimensions of the workpiece are provided in [26]. Milling was performed using both coated and bare WC four-edge fillet-end milling tools. The total cutting distance was 18 m and was divided into three equal-length stages. After each cutting stage, the notch wear and flank wear were analyzed with an optical microscope (OM). The detailed milling parameters and measurement instrument are provided in [26]. The flank wear was determined at three different locations on the

discontinuous edge flutes on the left and right sides of the tool (see Figure 3). The six flank wear measurements were averaged to derive a representative value for the tool. The maximum notch wear on both sides of the tool was also measured, and the average value was taken as the representative value for the tool.

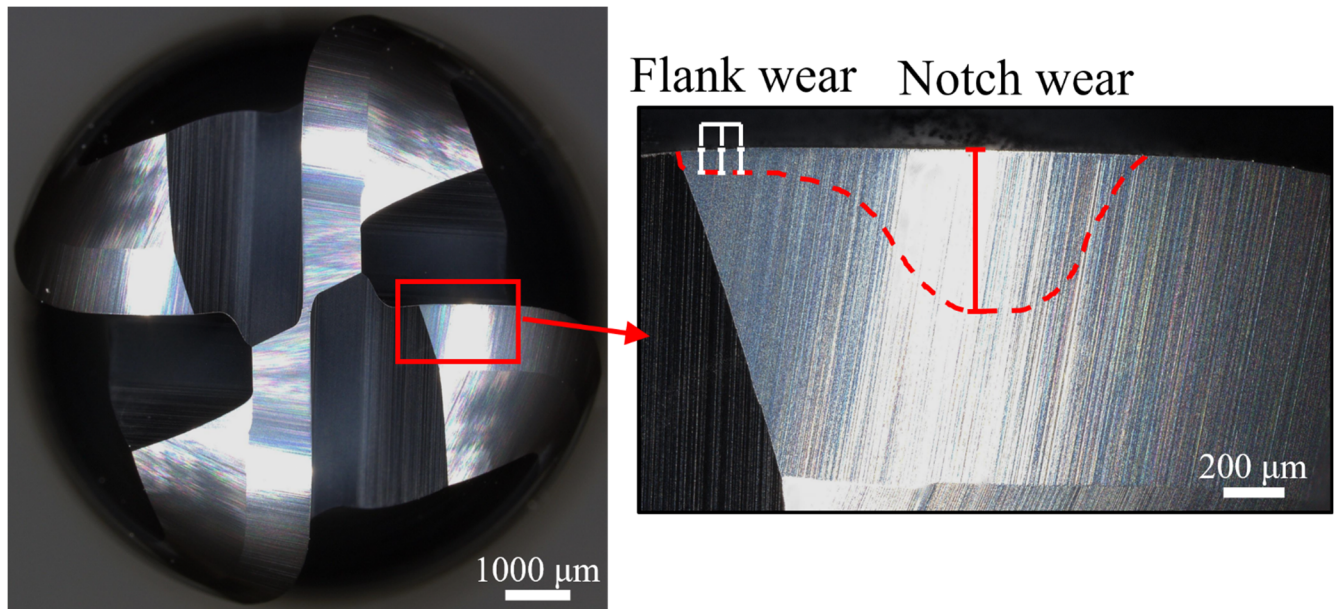


Figure 3. Schematic showing tool wear and notch wear measurement positions.

3. Results and Discussion

3.1. Chemical Composition

Figure 4a,b display the elemental content of both as-deposited and heat-treated (Al-CrNbSiTiMo)N films, respectively. Table 2 provides the exhaustive elemental content of the films, with an error range of 0.1–1.5 at.%. For the R_{N0} film, which contains no nitrogen, the compositions of the various elements are all within the range of 5–35 at.%, thereby meeting the definition of HEAs [1]. The R_{N33} , R_{N43} , R_{N50} , and R_{N56} films contain 42.8 at.%, 54.6 at.%, 57.3 at.% and 57.9 at.% nitrogen, respectively. That is, as the nitrogen flow ratio increases, the nitrogen content increases rapidly until the content reaches 54.6 at.% (R_{N43}) but then increases only very slowly as the nitrogen flow ratio is further increased (R_{N50} and R_{N56} films). It shows the same result with previous research [28,29,31], which showed that the nitrogen content in nitride HEA (HEAN) films saturates at a concentration of approximately 50 at.%. Metals readily form Me-N bonds with nitrogen [31], and this has a significant impact on the film properties. For example, as discussed in Section 3.4, the films exhibit increased hardness as the nitrogen content rises. As shown in Table 2, the as-deposited films contain a small amount of oxygen (~5–9 at.%). Oxides are often formed on metallic substrates or film surfaces [23]. In the present case, the O content is most likely the result of residual moisture in the deposition chamber and slight oxidation of the film surface following removal from the chamber.

The R_{N0} , R_{N33} , R_{N43} , R_{N50} , and R_{N56} films have relatively low oxygen contents of 9.5 at.%, 5.3 at.%, 5.2 at.%, 5.5 at.%, and 5.8 at.%, respectively. For the annealed HR_{N0} film, the oxygen content increases significantly to 54.3 at.% since the film lacks nitrogen, and hence metal element bonds are readily formed with oxygen. However, for the HEAN films, the oxygen content increases more moderately to 12.6 at.%, 8.9 at.%, 9.0 at.%, and 7.3 at.% for the HR_{N33} , HR_{N43} , HR_{N50} , and HR_{N56} films, respectively. When nitrogen is introduced during the deposition process, the binding reaction between the metallic elements and oxygen during the annealing process is effectively inhibited owing to the highly electronegative nature of nitrogen, which prompts the formation of strong Me-N

bonds. This reduces the spillover of nitrogen in the film and hence slows the formation of Me-O bonds, resulting in a low oxygen content [32]. The HR_{N0}, HR_{N33}, HR_{N43}, HR_{N50}, and HR_{N56} films have nitrogen contents of 0 at.%, 37.5 at.%, 50.3 at.%, 54.1 at.%, and 55.8 at.%, respectively. Namely, the nitrogen content in the annealed films is approximately 2–7 at.% lower than that in the as-deposited films. This finding is reasonable because the annealing process results in a slightly higher oxygen content, and hence the contents of all the other film elements, including nitrogen, are reduced.

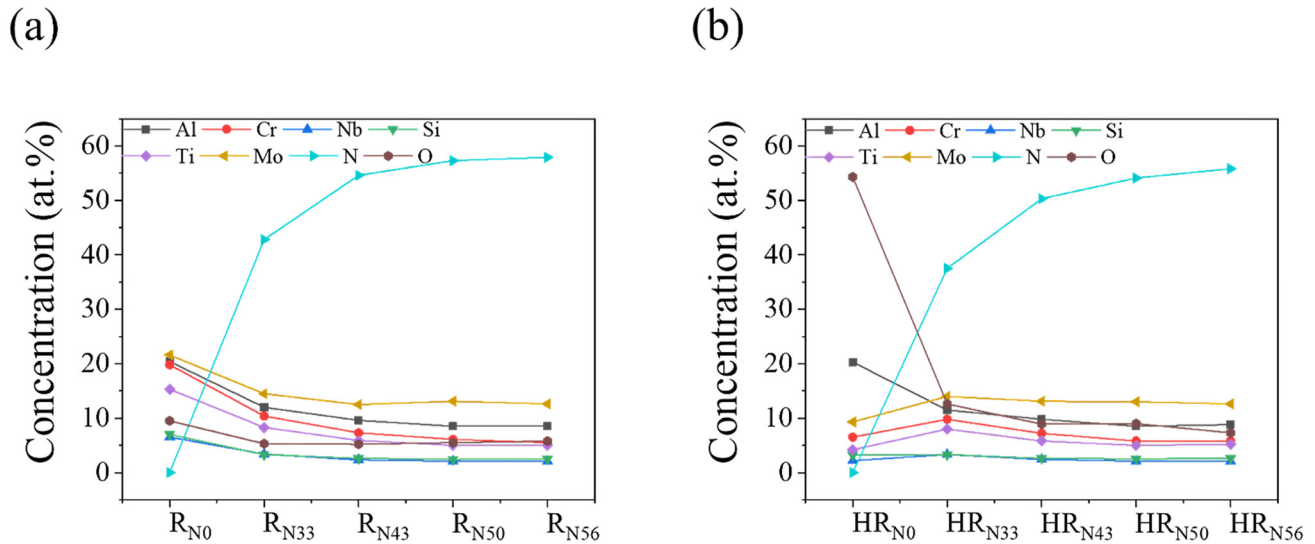


Figure 4. Element content of (a) as-sputtered and (b) heat-treated (AlCrNbSiTiMo)N films.

Table 2. Element compositions (at.%) of as-sputtered and heat-treated (AlCrNbSiTiMo)N films.

Film	N	O	Al	Si	Ti	Cr	Nb	Mo
R _{N0}	0	9.5 ± 0.3	20.4 ± 0.8	7.0 ± 0.3	15.3 ± 0.5	19.8 ± 0.3	6.5 ± 0.5	21.6 ± 1.2
R _{N33}	42.8 ± 0.8	5.3 ± 0.1	12.0 ± 0.5	3.3 ± 0.1	8.3 ± 0.2	10.4 ± 0.3	3.4 ± 0.3	14.5 ± 0.8
R _{N43}	54.6 ± 1.0	5.2 ± 0.4	9.6 ± 0.6	2.6 ± 0.1	5.9 ± 0.3	7.3 ± 0.7	2.3 ± 0.2	12.5 ± 0.6
R _{N50}	57.3 ± 1.2	5.5 ± 0.1	8.5 ± 0.7	2.4 ± 0.1	5.0 ± 0.4	6.1 ± 0.5	2.1 ± 0.1	13.1 ± 0.5
R _{N56}	57.9 ± 1.5	5.8 ± 0.1	8.6 ± 0.8	2.5 ± 0.1	5.0 ± 0.2	5.5 ± 0.4	2.1 ± 0.1	12.6 ± 0.7
HR _{N0}	0	54.3 ± 0.2	20.3 ± 0.1	3.2 ± 0.2	4.2 ± 0.2	6.5 ± 0.3	2.2 ± 0.2	9.3 ± 0.2
HR _{N33}	37.5 ± 0.9	12.6 ± 0.5	11.5 ± 0.2	3.3 ± 0.1	8.0 ± 0.2	9.8 ± 0.8	3.3 ± 0.1	14.0 ± 0.2
HR _{N43}	50.3 ± 0.6	8.9 ± 0.6	9.8 ± 0.2	2.6 ± 0.1	5.8 ± 0.6	7.2 ± 0.5	2.4 ± 0.2	13.1 ± 0.2
HR _{N50}	54.1 ± 0.4	9.0 ± 0.3	8.5 ± 0.2	2.5 ± 0.1	5.0 ± 0.5	5.8 ± 0.3	2.1 ± 0.1	13.0 ± 0.1
HR _{N56}	55.8 ± 0.5	7.3 ± 0.3	8.8 ± 0.1	2.6 ± 0.2	5.2 ± 0.4	5.8 ± 0.2	2.1 ± 0.2	12.6 ± 0.1

3.2. XRD and XPS Analyses

Figure 5 shows the XRD patterns for both the as-sputtered and heat-treated (AlCrNbSiTiMo)N films. The XRD pattern of the R_{N0} film shows a single broad peak, indicating that the film has an amorphous structure [31]. According to [6,33], large atomic size differences (around 0.020–0.030 nm) lead to severe lattice distortion, which is conducive to the formation of an amorphous structure [7,29]. In the alloys fabricated in the present study, the Al, Nb, and Ti elements have atomic radii of around 0.145 nm, the Cr element has an atomic radius of about 0.125 nm, and the Mo element has an atomic radius of approximately 0.140 nm. Moreover, the Si atoms in the substrate have a radius of approximately 0.117 nm. The atomic size mismatches between the various elements therefore range from 0.015 to 0.028 nm and hence favor the formation of an amorphous structure. For the R_{N33} film, prepared with the lowest nitrogen flow rate of 10 sccm, the XRD pattern contains no peaks other than those associated with the substrate. This finding indicates that a low nitrogen content induces a lattice strain (nitrogen solid solution), which prompts the formation of an

amorphous structure [34]. However, as the nitrogen flow rate increases, the films transition from an amorphous structure to a crystalline structure, as evidenced by the strong (111) signals in the XRD patterns of the R_{N43} , R_{N50} , and R_{N56} films. This change in the film structure is consistent with the findings of previous studies that the high-entropy effect of HEAs leads to the formation of simple FCC or BCC structures [3]. Binary nitrides such as TiN, NbN, and CrN exhibit FCC structures [34,35]. Therefore, it is reasonable to infer that the present (AlCrNbSiTiMo)N films also consist mainly of FCC structures. This inference is supported by the findings of [7,29,31], which indicate that HEAN films often show a prominent (111) diffraction peak and have an FCC structure.

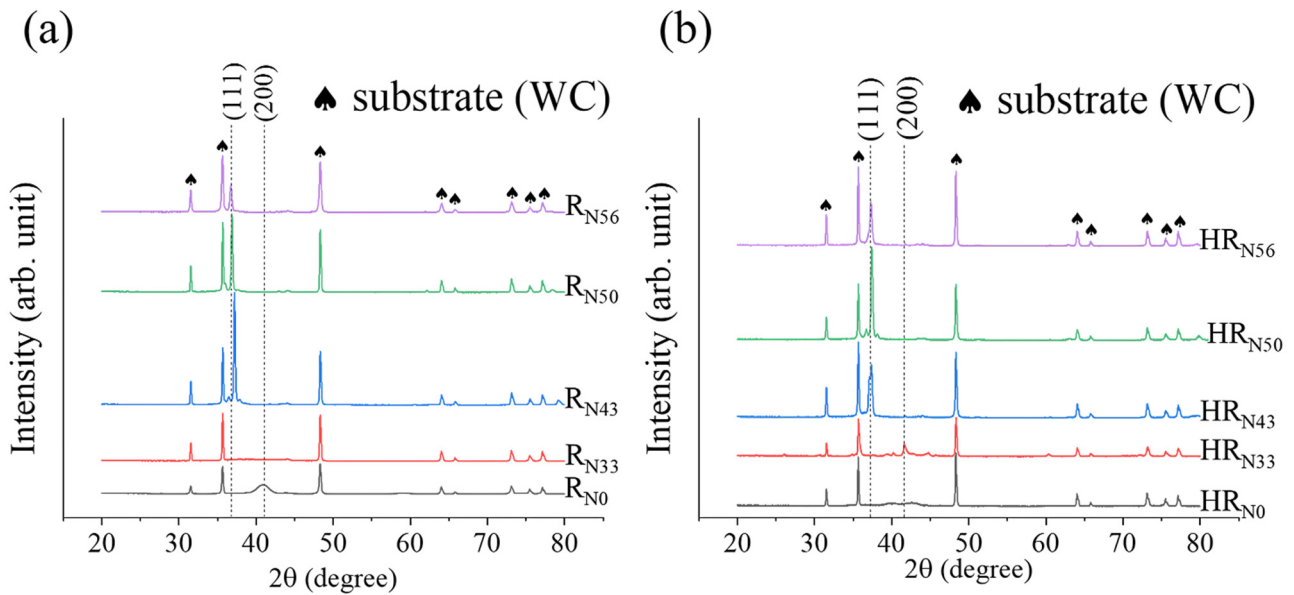


Figure 5. X-ray diffraction patterns of (a) as-sputtered and (b) heat-treated (AlCrNbSiTiMo)N films.

Figure 5b indicates that all the annealed HEAN films have a crystalline structure. Notably, even the HR_{N33} film, which is amorphous in the as-deposited condition, transforms into an FCC structure after annealing. This finding is reasonable because, according to [36], annealing treatment promotes structural transformation and then crystallization. For the HR_{N43} , HR_{N50} , and HR_{N56} films, the original prominent peak of (111) is maintained after annealing, and no other crystals are formed. Therefore, it can be inferred that the (AlCrNbSiTiMo)N films with a greater N element content (saturation state) have good thermal stability.

Tables 3–5 show the area percentages of the metal-metal (Me-Me), metal-oxygen (Me-O), and metal-nitrogen (Me-N) bonding areas in the (AlCrNbSiTiMo)N films. Table 4 additionally shows the bonding area percentages of MoO_2 and MoO_3 . For each film, the bonding percentages of the different bond types total 100%. For instance, the Si bonds in the R_{N43} film consist of 26.4% Si-Si bonds (see Table 3), 8.8% Si-O bonds (see Table 4), and 64.8% Si-N bonds (see Table 5). The R_{N33} film is dominated by Me-Me bonds (see Table 3), primarily Ti-Ti bonds (84.9%) and Cr-Cr bonds (74.9%). In other words, even though the deposition process is performed with nitrogen, the Me-N bonds contain only a small percentage of Si-N bonds (20.9%) (see Table 5). However, when the nitrogen flow rate is raised to 15 sccm, all the elements in the R_{N43} film form Me-N bonds. For the R_{N43} film, the area percentage of the Me-N bonds ranges from 39.5% to 52.6%. For the R_{N50} film, the Me-N bonding area percentage ranges from 53.9% to 77.3%. Moreover, for the R_{N56} film, the area percentage ranges from 60.2% to 78.8%. In other words, the amount of Me-N bonds increases as the N content increases.

Table 3. X-ray photoelectron spectroscopy analysis results for area percentages of metal–metal (Me–Me) bonding in as-sputtered and heat-treated (AlCrNbSiTiMo)N films.

Film Code	Proportion of Me–Me Bonds (%)					
	Al	Si	Ti	Cr	Nb	Mo
R _{N0}	-	72.7	63.1	19.3	-	61.3
R _{N33}	-	70.3	84.9	74.8	53.0	67.9
R _{N43}	-	26.4	46.0	36.8	2.8	-
R _{N50}	-	22.7	22.8	25.3	-	-
R _{N56}	-	21.2	23.8	22.5	-	-
HR _{N0}	-	-	43.2	11.8	-	66.5
HR _{N33}	-	35.1	19.2	30.7	46.0	85.4
HR _{N43}	-	-	-	-	-	-
HR _{N50}	-	-	-	-	-	-
HR _{N56}	-	-	-	-	-	-

Table 4. X-ray photoelectron spectroscopy analysis results for area percentages of metal–oxygen (Me–O) bonding in as-sputtered and heat-treated (AlCrNbSiTiMo)N films. Note: Al–O bonding corresponds to Al₂O₃; Si–O bonding is associated with SiO₂; Ti–O bonding corresponds to TiO₂; Cr–O bonding includes Cr₂O₃ and CrO₃; Nb–O bonding refers to NbO₂ and Nb₂O₅.

Film Code	Bonding Proportion (%)						
	Me–O					Mo–O	
	Al	Si	Ti	Cr	Nb	MoO ₂	MoO ₃
R _{N0}	100	27.3	36.9	80.7	100	38.7	-
R _{N33}	100	8.8	15.1	25.2	47.0	32.1	-
R _{N43}	60.5	8.8	11.5	19.9	44.6	-	48.2
R _{N50}	46.1	0	17.6	13.4	42.8	-	41.0
R _{N56}	38.7	0	7.8	14.0	39.8	-	36.9
HR _{N0}	100	100	56.8	88.2	100	2.9	30.6
HR _{N33}	100	64.9	59.7	69.3	54.0	-	14.4
HR _{N43}	100	35.9	33.4	43.0	42.1	-	36.1
HR _{N50}	100	35.5	29.9	26.6	30.2	-	24.4
HR _{N56}	100	14.6	12.4	29.4	29.2	-	25.5

Table 5. X-ray photoelectron spectroscopy analysis results for area percentages of metal–nitrogen (Me–N) bonding in as-sputtered and heat-treated (AlCrNbSiTiMo)N films. Note: Al–N bonding corresponds to AlN; Si–N bonding is associated with Si₃N₄; Ti–N bonding corresponds to TiN; Cr–N bonding includes CrN and Cr₂N; Nb–N bonding refers to NbN; Mo–N bonding refers to MoN.

Film Code	Proportion of Me–N Bonds (%)					
	Al–N	Si–N	Ti–N	Cr–N	Nb–N	Mo–N
R _{N0}	-	-	-	-	-	-
R _{N33}	-	20.9	-	-	-	-
R _{N43}	39.5	64.8	42.5	43.3	52.6	51.8
R _{N50}	53.9	77.3	59.6	61.3	57.2	59
R _{N56}	61.3	78.8	68.4	63.5	60.2	63.1
HR _{N0}	-	-	-	-	-	-
HR _{N33}	-	-	21.1	-	-	-
HR _{N43}	-	64.1	66.6	57	57.9	63.9
HR _{N50}	-	64.5	70.1	73.4	69.8	75.6
HR _{N56}	-	85.4	87.6	70.6	70.8	74.5

The HR_{N0} film consists mainly of Me–O bonds (see Table 4), such as Al–O (100%), Si–O (100%), Ti–O (56.8%), Cr–O (88.2%), Nb–O (100%), and Mo–O (33.5%). The HR_{N33} film also contains a large number of Me–O bonds, with all the bonding area percentages exceeding 54%, except for the Mo–O bond (14.4%).

The large percentage of Me-O bonds in the two films can be attributed to their high oxygen contents of 54.3 at.% and 12.6 at.%, respectively (see Table 2). For the annealed films produced with an increased nitrogen flow rate (HR_{N43}, HR_{N50}, and HR_{N56}), the percentage of Me-N bonds is generally significantly higher (more than 57%) than that in the corresponding as-deposited films (see Table 5). For the annealed HR_{N33} film, 20.9% of the Si-N bonds in the as-deposited R_{N33} film disappear after annealing. This finding is consistent with the observation of [37] that heat treatment at temperatures greater than 900 °C causes the destruction of the Si-N bonds in films with a low nitrogen content. However, as the nitrogen content saturates (i.e., the HR_{N43}, HR_{N50}, and HR_{N56} films), the percentage of Si-N bonds remains over 64%. The finding that the number of Me-N bonds generally increases after annealing is consistent with the assertion of Yeh et al. [8] that the greater thermal energy produced in high-temperature environments promotes the binding of metallic elements to nitrogen.

Interestingly, in all the annealed films, aluminum exists exclusively in the form of Al-O bonds. In other words, no Al-N bonds or Al-Al bonds are formed (see Table 4). Cai et al. [38] demonstrated that the incorporation of Al into nitrogen-containing films enhances the thermal properties by facilitating the formation of a protective aluminum oxide layer on the surface of the film. Additionally, Ougier et al. [39] indicated that an uninterrupted and dense Al₂O₃ layer on the surface of heat-treated Cr₂AlC films acts as an effective barrier to the diffusion of oxygen. Therefore, the annealed films in the present study are expected to exhibit superior oxidation resistance and thermal durability. As shown in Table 4, neither the R_{N0} film nor the R_{N33} film contains any MoO₃ phase. However, the R_{N43}, R_{N50}, and R_{N56} films have MoO₃ bond contents of 48.2, 41.0, and 36.9%, respectively. After annealing, all the annealed films contain MoO₃ bonds, with MoO₃ bonding percentages of 30.6, 14.4, 36.1, 24.4, and 25.5% for the HR_{N0}, HR_{N33}, HR_{N43}, HR_{N50}, and HR_{N56} films, respectively. Among all the films, the as-deposited R_{N43} film and annealed HR_{N43} film contain the greatest number of MoO₃ bonds (48.2% and 36.1%, respectively). The formation of MoO₃ as a solid lubricant significantly decreases the COF of films during sliding [21]. Therefore, the X-ray photoelectron spectroscopy analysis results for the MoO₃ phase in Table 4 indicate that both the R_{N43} film and the HR_{N43} film are expected to possess superior tribological characteristics (as further discussed in Section 3.5).

3.3. Cross-Sectional and Surface Morphologies

SEM cross-sectional graphics of all the (AlCrNbSiTiMo)N films are shown in Figure 6. It is important to mention that the as-sputtered films were applied to silicon substrates, whereas the heat-treated films were applied to WC disks. This change was necessary because the films peeled off the Si substrates when subjected to the high annealing temperature of 950 °C. The R_{N0} film shows a featureless cross-sectional structure with relatively rough features (see Figure 6a). By contrast, the cross-sectional structure of the R_{N33} film has a flaky appearance (see Figure 6c). However, when the nitrogen flux exceeds 15 sccm, the cross-sectional morphology transitions into a clearly defined columnar morphology, as illustrated in Figure 6e,g,i for the R_{N43}, R_{N50}, and R_{N56} films, respectively. This finding is reasonable because all three films have a nitrogen content of more than 54.6 at.% (see Table 2) and are thus expected to have a column structure [28]. Regarding the annealed films, the HR_{N0} film changes from an original rough and featureless cross-sectional structure to a denser cross-sectional structure (see Figure 6b). Similarly, the HR_{N33} film changes from a flaky structure to a denser structure (see Figure 6d). However, the R_{N43}, R_{N50}, and R_{N56} all maintain their original obvious columnar structures, as shown in Figure 6f,h,j, respectively. Comparing the annealed films with their as-deposited counterparts, it can be seen that the annealing process reduces some of the gaps between the columnar features, thereby increasing the density of the annealed structure. The present findings are thus consistent with those of Liang et al. [40], who showed that the gaps in films tend to be eliminated in high-temperature environments because of the enhanced atomic diffusivity, which helps fill the pores and voids, ultimately leading to smoother growth.

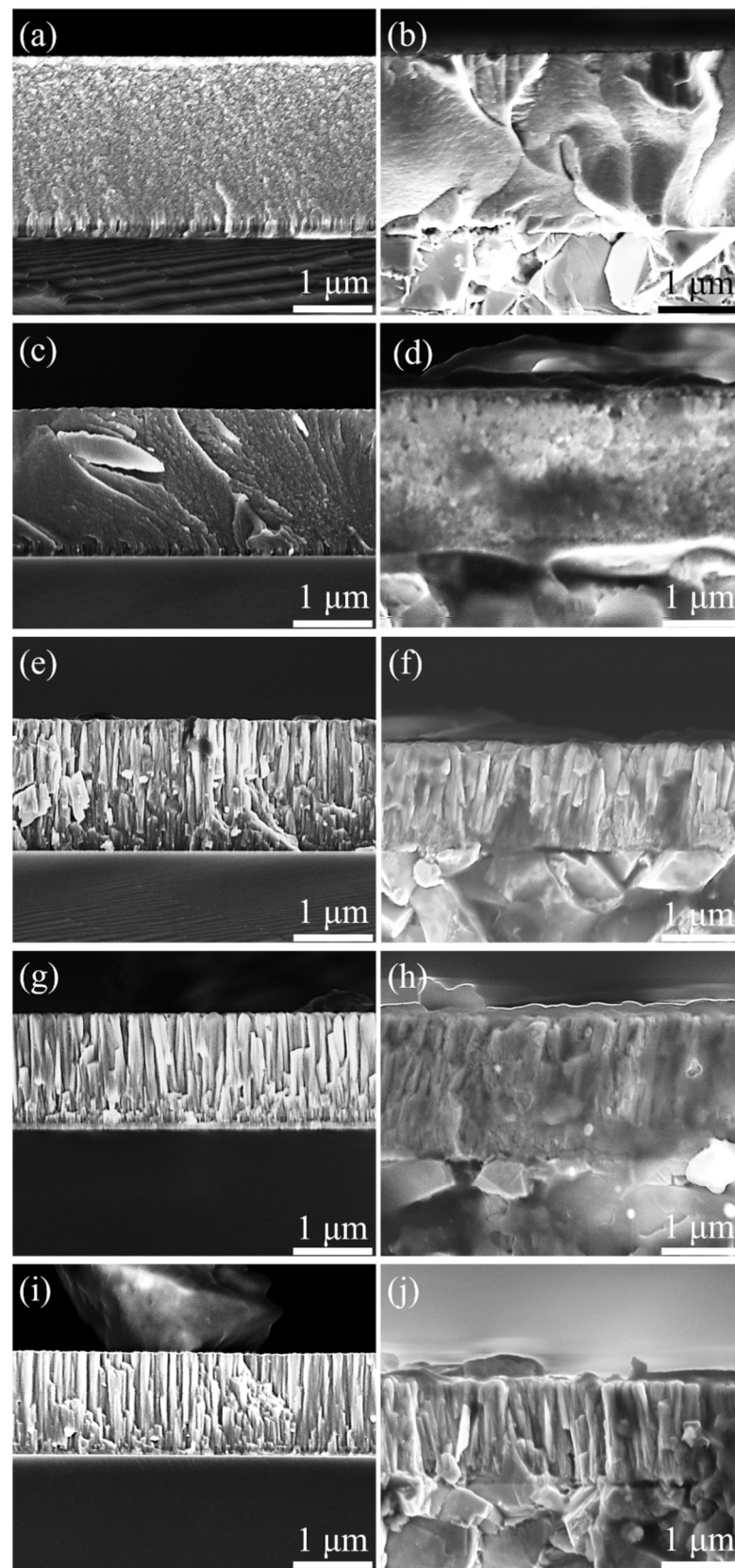


Figure 6. Cross-section SEM graphics of (AlCrNbSiTiMo)N films: (a) R_{N0}, (b) HR_{N0}, (c) R_{N33}, (d) HR_{N33}, (e) R_{N43}, (f) HR_{N43}, (g) R_{N50}, (h) HR_{N50}, (i) R_{N56}, and (j) HR_{N56}.

Table 6 shows that the thickness of the as-deposited films reduces from 2.19 μm (R_{N0}) to 1.28 μm (R_{N56}) as the nitrogen flow rate increases. The reduction in the film thickness is likely attributed to the deposition of nitrogen-containing compounds on the target surface under high-nitrogen conditions. The resulting target poisoning effect decreases the sputter yield, reducing the deposition rate and consequently leading to a thinner film [31,41].

Table 6. Hardness (H), elastic modulus (E), ratio of H/E, roughness, thickness, and adhesion strength of as-deposited and annealed (AlCrNbSiTiMo)N films.

Film	Hardness (GPa)	Elastic Modulus (GPa)	H/E Ratio	Roughness Ra (nm)	Thickness (μm)	Adhesion Strength Lc (N)
R_{N0}	17.4 ± 1.0	622.9 ± 35.3	0.028	21.2 ± 1.2	2.19	61.3
R_{N33}	23.5 ± 2.1	602.4 ± 35.0	0.039	28.5 ± 1.3	1.78	48.6
R_{N43}	33.0 ± 2.3	496.5 ± 40.3	0.066	23.0 ± 1.3	1.59	>100
R_{N50}	28.0 ± 1.1	550.2 ± 23.4	0.051	20.8 ± 2.5	1.41	>100
R_{N56}	25.5 ± 2.6	562.1 ± 47.2	0.045	19.5 ± 1.1	1.28	>100
HR_{N0}	20.0 ± 1.1	467.9 ± 36.4	0.043	39.2 ± 4.0	2.33	39
HR_{N33}	24.0 ± 1.4	711.7 ± 34.9	0.034	45.3 ± 2.0	1.89	11.1
HR_{N43}	36.0 ± 1.6	498.9 ± 56.2	0.072	29.3 ± 1.8	1.46	>100
HR_{N50}	29.5 ± 1.0	714.0 ± 31.3	0.041	29.6 ± 1.7	1.43	61.6
HR_{N56}	28.9 ± 1.6	719.6 ± 42.5	0.040	28.3 ± 1.7	1.31	47.3

After annealing, the thicknesses of the HR_{N0} and HR_{N33} films increase (from 2.19 to 2.33 μm and 1.78 to 1.89 μm , respectively). In contrast, the thickness of the HR_{N43} film decreases from 1.59 to 1.46 μm . Meanwhile, the thicknesses of the HR_{N50} and HR_{N56} films increase slightly, from 1.41 to 1.43 μm and from 1.28 to 1.31 μm , respectively. In other words, all of the films, except for the HR_{N43} film, become thicker after the annealing process. This is likely a result of the development of an oxide layer on the surface of film at raised temperatures. For instance, the O contents of the HR_{N0} (54.3 at.%) and HR_{N33} (12.6 at.%) films are significantly higher than those of the R_{N0} (9.5 at.%) and R_{N33} (5.3 at.%) films. Thus, the two films undergo an obvious increase in thickness (around 0.14 μm and 0.11 μm , respectively). For the HR_{N50} and HR_{N56} films, only slight oxidation occurs during annealing (i.e., O contents of 9.0 and 7.3 at.%, respectively). Consequently, the film thickness shows a more moderate increase of 0.02 μm and 0.03 μm , respectively. Previous studies on the increased thickness of HEAN films following annealing have suggested several reasons for the smaller increase in films with a higher N content. First, nitrogen possesses high electronegativity, which allows it to readily form strong Me-N bonds with metals [32]. These bonds prevent nitrogen from escaping during annealing and hence reduce the formation of Me-O bonds. Second, the increased thermal energy in high-temperature environments strengthens the Me-N bonds in the film, further reducing the possibility of nitrogen escape [8]. Finally, when the nitrogen content of the film reaches approximately 50%, only a thin oxide layer is formed under high-temperature annealing (~ 1000 °C) because films with a saturated nitrogen composition exhibit excellent oxidation resistance and thermal stability [42].

Interestingly, the thickness of the HR_{N43} film decreases from 1.59 to 1.46 μm after annealing. This does not necessarily indicate the absence of oxidation during the annealing process. Indeed, according to the Me-O bonding analysis results in Table 4, the Me-O bonding ratio of the HR_{N43} film is significantly higher than that of the R_{N43} film, which suggests the formation of an oxide layer. However, the thickness measurement results show that the oxide layer is very thin. Previous research [43] found that the thickness of films is positively correlated with the crystallographic strength of the film structure. Moreover, a higher crystallinity leads to a greater intensity of the XRD pattern and a narrower full width at half maximum (FWHM) [44]. For the R_{N43} film, the XRD pattern shows a strong diffraction peak associated with (111) crystalline phase (see Figure 5a). However, the intensity of the diffraction peak decreases significantly after annealing (see Figure 5b). The peak intensity and FWHM of the R_{N43} film are 121 and 0.219 nm, respectively, whereas

those of the HR_{N43} film are 44 and 0.408 nm, respectively. It is speculated that this reduction in the peak intensity explains the lower thickness of the HR_{N43} film. In general, the results suggest that the thickness of HEAN films after annealing depends not only on the degree of oxidation but also on the change in the peak intensity of the crystalline phase.

Figure 7 shows the SEM surface graphics of the as-sputtered (AlCrNbSiTiMo)N films and annealed (AlCrNbSiTiMo)N films. The as-sputtered R_{N0} and R_{N33} films exhibit strip-like cluster morphologies (see Figure 7a,c). By contrast, the as-deposited R_{N43}, R_{N50}, and R_{N56} films have cone-shaped cluster structures (see Figure 7e,g,i). This observation is consistent with the finding of Liang et al. [43] that a greater nitrogen flow rate is associated with a gradual tapering of the surface clusters. After the heat treatment, the surface morphology of the HR_{N0} film is relatively dense (see Figure 7b). Moreover, the surface morphology of the HR_{N33} film becomes blurred (see Figure 7d). The HR_{N43}, HR_{N50}, and HR_{N56} films have similar cone-shaped cluster-like surface morphologies (see Figure 7f,h,j).

As shown in Table 6, the R_{N0}, R_{N33}, R_{N43}, R_{N50}, and R_{N56} films had surface roughness values of 21.2 nm, 28.5 nm, 23.0 nm, 20.8 nm, and 19.5 nm, respectively. After annealing, the surface roughness increased to 39.2 nm, 45.3 nm, 29.3 nm, 29.6 nm, and 28.3 nm, respectively, as a result of the formation of an oxidation layer on the film surface in the high-temperature environment. The increase in the surface roughness is especially noticeable for the HR_{N0} and HR_{N33} films (i.e., from 21.2 nm to 39.2 nm and 28.5 nm to 45.3 nm, respectively). According to Table 2, the HR_{N0} and HR_{N33} films have high oxygen contents of 54.3 and 12.6 at.%, indicating the occurrence of severe oxidation. By contrast, the HR_{N43}, HR_{N50}, and HR_{N56} films have O contents of 8.9, 9.0, and 7.3 at.%, respectively, indicating more moderate oxidation and hence a smaller increase in the surface roughness (6.3–8.8 nm).

3.4. Mechanical Properties

Table 6 also lists the mechanical properties of the films. Of all the as-deposited films, the R_{N0} film exhibits the lowest hardness (17.4 GPa). As the nitrogen flow rate increases to 10 and 15 sccm, the hardness of the R_{N33} and R_{N43} films increases to 23.5 and 33.0 GPa, respectively. The increased hardness is due to the development of a greater quantity of high-hardness nitrides and the incorporation of N atoms into the film, which promotes the formation of high-strength Me-N bonds [29]. An increased nitrogen flow rate further increases the insertion of N atoms into the lattice, thereby reinforcing the interstitial solid-solution strengthening effect [45,46]. The incorporation of substitutional Mo atoms further improves the solid-solution strengthening effect [22]. However, for the R_{N50} and R_{N56} films, the hardness decreases with an increasing nitrogen flow rate, falling to 28.0 GPa and 25.5 GPa, respectively. For these films, the nitrogen content saturates, and a higher nitrogen flow rate results in target poisoning and the formation of nitrides on the target surface. This not only leads to a lower film deposition rate but also causes defects such as columnar coarse crystals and pores in the film, which degrade the film quality and lower the film hardness. Similar results have been reported by Liang et al. [29] and Cui et al. [31]. For all the annealed films, the hardness exceeds that of the as-deposited films. Specifically, the HR_{N0}, HR_{N33}, HR_{N43}, HR_{N50}, and HR_{N56} films have hardness levels of 20.0, 24.0, 36.0, 29.5, and 28.9 GPa, respectively, corresponding to a hardness improvement range of approximately 1–4 GPa. The increased hardness of the annealed films stems mainly from the densification of the annealed film structure, as described in Section 3.3. According to Lin et al. [9], densification plays an important role in improving the hardness by eliminating internal defects such as cracks and pores within the film structure. The low interstitial concentration resulting from the higher film density then leads to a higher hardness. Therefore, even the HR_{N0} film with no nitrogen and the HR_{N33} film with only a small amount of nitrogen show an improved hardness following annealing because of their dense structures. The enhanced hardness of the annealed films can also be attributed to the increased thermal energy generated during high-temperature annealing, which promotes the total bonding strength between the nitrogen and target components [8]. This is evidenced by the X-ray photoelectron spectroscopy analysis outcomes in Table 5, which

display that the Me-N bonding area percentages of the annealed HR_{N43} , HR_{N50} , and HR_{N56} films are greater than those of the as-deposited R_{N43} , R_{N50} , and R_{N56} films.

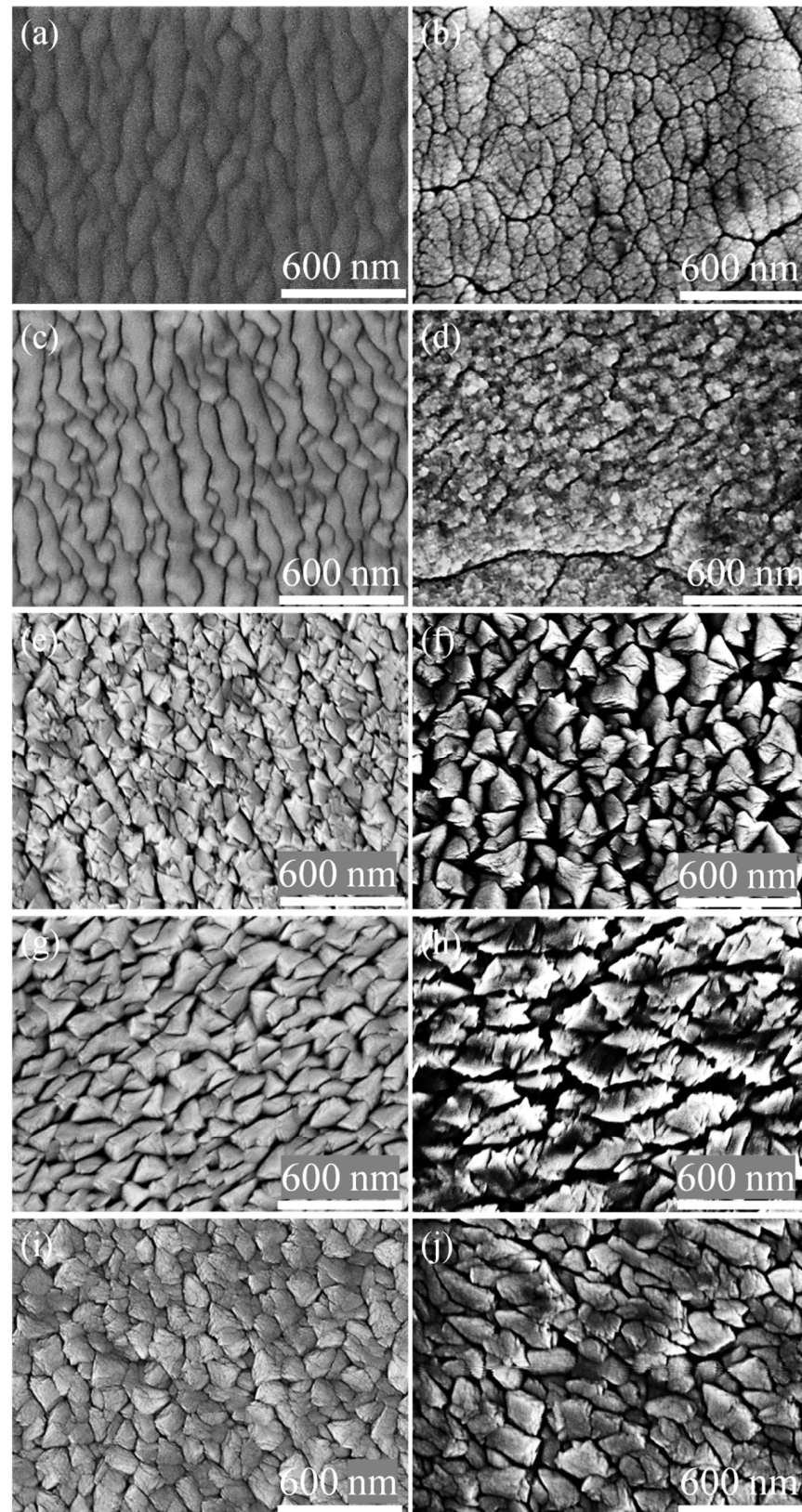


Figure 7. SEM surface graphics of (AlCrNbSiTiMo)N films: (a) R_{N0} , (b) HR_{N0} , (c) R_{N33} , (d) HR_{N33} , (e) R_{N43} , (f) HR_{N43} , (g) R_{N50} , (h) HR_{N50} , (i) R_{N56} , and (j) HR_{N56} .

Generally, the adhesion strength is a crucial indicator of the protection capability and durability of films. The adhesion strength affects the stability of the film under different environments and stresses, and is critical for ensuring the performance of the film during use [47]. Table 6 displays the adhesion strengths of the as-sputtered and heat-treated (AlCrNbSiTiMo)N films. As detailed in Section 2.2, the critical load represents the load at which the film begins to peel away from the substrate during the scratch test. In Figure 8, optical microscopy (OM) graphics depict the scratch track present on the R_{N33} film surface. It is observed that the film begins to detach from the substrate when the tip load reaches 48.6 N. Therefore, the critical load (L_c) of the film is established as 48.6 N. As shown in Table 6, the R_{N0} and R_{N33} films have relatively low critical loads of 61.3 N and 48.6 N, respectively. However, the R_{N43} , R_{N50} , and R_{N56} films exhibit critical loads higher than 100 N. The hardness of the various films is correlated with their structures. In particular, the R_{N0} and R_{N33} films have amorphous structures and a lower hardness, while the R_{N43} , R_{N50} , and R_{N56} films have FCC structures and a higher hardness. The grain boundaries in crystals play an important role in resisting plastic deformation. Therefore, a high adhesion strength is associated with a crystalline rather than amorphous structure [48]. After annealing treatment, the HR_{N43} film maintains an outstanding adhesion strength ($L_c > 100$ N). Nevertheless, the critical load capacities of all the other films (HR_{N0} , HR_{N33} , HR_{N50} , and HR_{N56}) reduce to 39 N, 11.1 N, 61.6 N, and 47.3 N, respectively. According to [49], the reduction in the critical load of $Cr_{(1-x)}Al_xN$ films after the heat treatment is attributed to the high interfacial stress caused by a mismatch between the coefficients of thermal expansion (CTE) of the substrate and film. The superior adhesion strength of the HR_{N43} film is consistent with the view of Leyland and Matthews [50] that films with a higher ratio of hardness-to-elastic modulus (H/E ratio) are capable of absorbing more energy before failure, which reduces the likelihood of fracturing during scratch tests. Table 6 shows that, among all the films, the HR_{N43} film has the highest H/E ratio both before (0.066) and after annealing (0.072). Thus, it has an enhanced ability to absorb elastic energy in process the scratch testing and therefore exhibits a higher adhesion strength ($L_c > 100$ N).

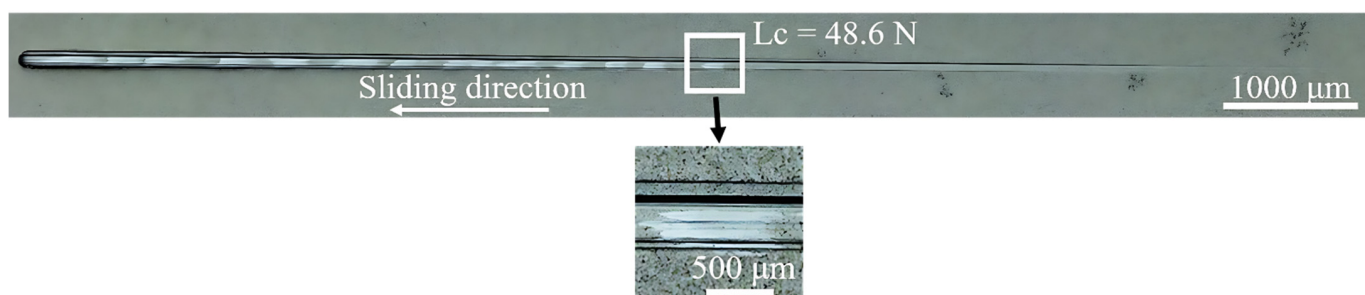


Figure 8. OM graphics of scratch track on R_{N33} film.

3.5. Tribological Performance

3.5.1. Friction Performance

Figure 9a,b present the COF curves for the as-sputtered and after the heat treatment (AlCrNbSiTiMo)N films while sliding against the Si_3N_4 balls. For comparison, the two figures also show the COF curves for the original WC substrate and heat-treated WC substrate. As illustrated in Figure 9a, the COF curve of the WC substrate is relatively smooth and the value is 0.19. The R_{N0} and R_{N33} films show extremely high COFs in the first 400 and 200 sliding cycles, respectively. However, after this running-in period, the COF of the R_{N33} film decreases abruptly and remains constant at approximately 0.16 thereafter. As described above, the R_{N33} film has a low adhesion strength ($L_c = 48.6$ N). Thus, it rapidly fractures during the running-in period and produces broken worn debris, which leads to a higher and oscillating COF. However, as the sliding process continues, the worn debris is gradually removed from the sliding interface and does not adhere to the wear track.

Consequently, the COF falls rapidly and then remains approximately constant. For the R_{N0} film, the high and oscillating COF in the running-in stage is the result of adhesion wear at the contact surface, which causes some material from the Si_3N_4 ball and some worn debris from the film to adhere to the worn surface (see Section 3.5.3). This adhesion behavior causes the surface to roughen, which leads to a relatively high and oscillating COF following the initial running-in period. The R_{N43} , R_{N50} , and R_{N56} films show smooth and stable friction curves throughout the wear test, with average COFs of 0.17, 0.15, and 0.15, respectively. The low and smooth COF curves is caused by the formation of MoO_3 solid lubricant in the film [22]. The XPS results in Table 4 support this statement, which indicate that the three films possess relatively high proportions of MoO_3 bonds (48.2%, 41.0%, and 36.9%, respectively), whereas the R_{N0} and R_{N33} films have no MoO_3 bonds and thus no MoO_3 solid lubricant.

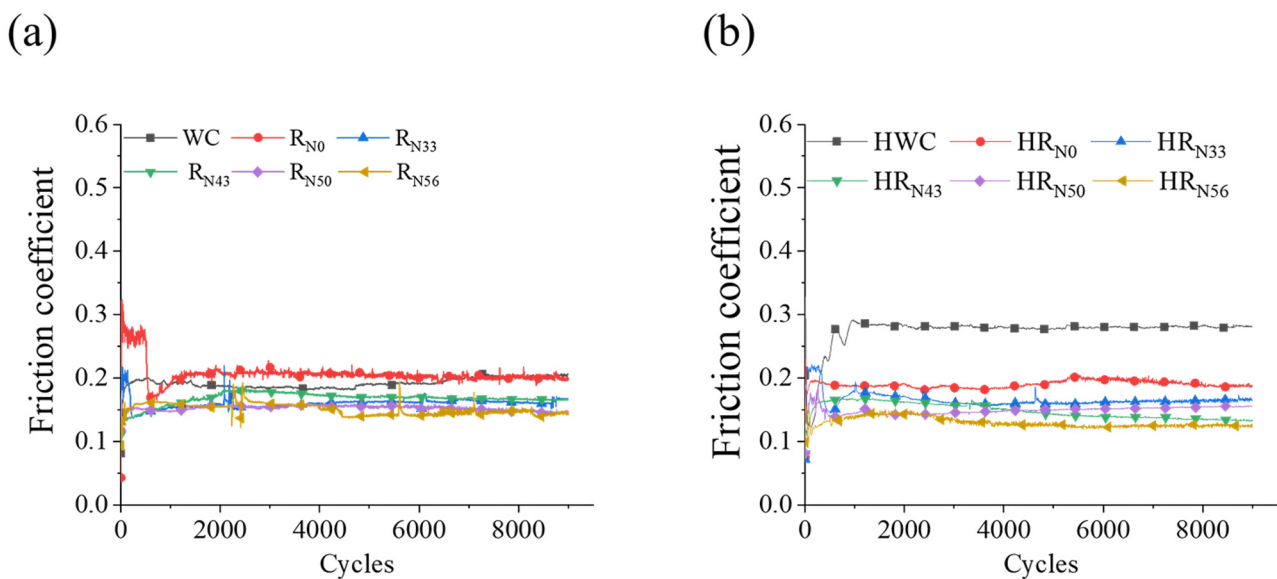


Figure 9. Curves of COF for (a) as-deposited (AlCrNbSiTiMo)N films and substrate (WC), and (b) annealed (AlCrNbSiTiMo)N films and substrate (WC).

Figure 9b shows that the annealed HWC substrate has a significantly greater COF (0.28) than the original WC substrate (0.19) due to its higher surface roughness ($R_a = 52.7$ nm vs. $R_a = 16.0$ nm). However, all the annealed films show a smoother COF curve than their as-deposited counterparts. This can be attributed to the formation of MoO_3 and Al_2O_3 during annealing (see Table 4). Notably, all the annealed films have a 100% Al bonding area percentage (Al_2O_3 phase). According to [51,52], Al_2O_3 effectively reduces the COF of films because it acts as a solid lubricant that reduces the shear resistance at the sliding surface. The COFs of the HR_{N0} , HR_{N33} , HR_{N43} , HR_{N50} , and HR_{N56} films (0.19, 0.16, 0.15, 0.15, and 0.13) are thus below those of the equivalent as-sputtered films (0.21, 0.16, 0.17, 0.15, and 0.15).

3.5.2. Wear Properties

Table 7 lists the worn depth and worn rate for all the films, as well as the WC and HWC substrates. The worn depth of the WC substrate is just 0.23 μm , accompanied by a worn rate of 0.96×10^{-6} $mm^3/(N \times m)$. Among all the as-deposited films, the R_{N0} film, with no nitrogen addition, has the highest worn depth (2.20 μm) and worn rate (18.25×10^{-6} $mm^3/(N \times m)$). For the R_{N33} film, the worn depth and worn rate fall slightly to 2.11 μm and 15.77×10^{-6} mm^3/Nm , respectively, due to its higher hardness (23.5 GPa) and H/E ratio (0.039). However, the worn depths of the R_{N0} and R_{N33} films are both higher than the film thickness (2.06 μm and 1.78 μm , respectively). This suggests that both films are worn away during the sliding process, and the wear scar penetrates the underlying substrate. This assertion is

reasonable because the R_{N0} and R_{N33} films both possess low adhesion strength, low hardness, and no MoO_3 solid lubricant, resulting in reduced wear resistance. For the R_{N43} film, the worn depth and worn rate fall significantly to $0.15 \mu\text{m}$ and $0.49 \times 10^{-6} \text{mm}^3/\text{Nm}$, respectively. As shown in Table 6, the R_{N43} film possesses the highest hardness (33.0 GPa) and highest H/E ratio (0.066) of all the as-deposited films. According to [50], a high H/E ratio typically indicates a better wear resistance. Additionally, Table 4 shows that the R_{N43} film forms the largest amount of MoO_3 solid lubricant among all the as-deposited films (48.2%), which is beneficial for further reducing the worn rate and worn depth. For the R_{N50} and R_{N56} films, prepared with higher N_2 flow rates of 20 and 25 sccm, the worn depths increase slightly to $0.20 \mu\text{m}$ and $0.41 \mu\text{m}$, respectively, while the worn rates increase to $0.49 \times 10^{-6} \text{mm}^3/(\text{N} \times \text{m})$ and $0.75 \times 10^{-6} \text{mm}^3/(\text{N} \times \text{m})$. The poorer wear resistance of the R_{N50} and R_{N56} films is reasonable due to their lower hardness (28.0 and 25.5 GPa, respectively) and H/E ratio (0.051 and 0.045, respectively) than the R_{N43} film. Nonetheless, the tribological properties of the two films are still better than those of the R_{N0} and R_{N33} films.

Table 7. COF, worn depth, and worn rate of as-deposited and annealed (AlCrNbSiTiMo)N films and substrate (WC) against Si_3N_4 counterbody.

Film	COF	Worn Depth (μm)	Worn Rate ($10^{-6} \text{mm}^3/(\text{N} \times \text{m})$)
WC	0.19	0.23 ± 0.03	0.96 ± 0.25
R_{N0}	0.21	2.20 ± 0.13	18.25 ± 1.45
R_{N33}	0.16	2.11 ± 0.06	15.77 ± 1.07
R_{N43}	0.17	0.15 ± 0.01	0.49 ± 0.05
R_{N50}	0.15	0.20 ± 0.01	0.75 ± 0.03
R_{N56}	0.15	0.41 ± 0.03	1.45 ± 0.10
HWC	0.28	0.25 ± 0.01	1.14 ± 0.10
HR_{N0}	0.19	0.22 ± 0.03	1.02 ± 0.08
HR_{N33}	0.16	1.93 ± 0.05	16.67 ± 0.77
HR_{N43}	0.15	0.10 ± 0.01	0.48 ± 0.07
HR_{N50}	0.15	1.75 ± 0.06	9.88 ± 0.36
HR_{N56}	0.13	1.19 ± 0.08	8.29 ± 0.94

After annealing, the worn depth and worn rate of the WC substrate that after the heat treatment remain very close to those of the original WC substrate (i.e., $0.25 \mu\text{m}$ and $1.14 \times 10^{-6} \text{mm}^3/(\text{N} \times \text{m})$ (HWC) vs. $0.23 \mu\text{m}$ and $0.96 \times 10^{-6} \text{mm}^3/(\text{N} \times \text{m})$ (WC)). The annealing process increases the surface roughness from 19.3 nm (WC) to 52.7 nm (HWC) and the COF from 0.19 (WC) to 0.28 (HWC). However, the hardness barely changes (15.8 GPa vs. 15.6 GPa). This indicates that the HWC substrate has excellent thermal stability, allowing it to effectively retain its wear resistance. The HR_{N0} film exhibits considerably lower worn depth and worn rate ($0.22 \mu\text{m}$ and $1.02 \times 10^{-6} \text{mm}^3/(\text{N} \times \text{m})$) than the original R_{N0} film ($2.20 \mu\text{m}$ and $18.25 \times 10^{-6} \text{mm}^3/(\text{N} \times \text{m})$, individually). For the HR_{N33} film, the worn depth reduces slightly compared to the non-annealed film ($1.93 \mu\text{m}$ (HR_{N33}) vs. 2.11 (R_{N33})) while the worn rate increases ($16.67 \times 10^{-6} \text{mm}^3/(\text{N} \times \text{m})$ (HR_{N33}) vs. $15.77 \times 10^{-6} \text{mm}^3/(\text{N} \times \text{m})$ (R_{N33})). However, the worn depth ($1.93 \mu\text{m}$) is larger than the film thickness ($1.89 \mu\text{m}$). This indicates that the HR_{N33} film wears through completely during the sliding process, and the wear scar penetrates into the substrate. The HR_{N43} film shows the lowest worn depth ($0.10 \mu\text{m}$) and worn rate ($0.48 \times 10^{-6} \text{mm}^3/(\text{N} \times \text{m})$) of all the films (both annealed and as-deposited). Finally, the HR_{N50} and HR_{N56} films have worn depths of $1.75 \mu\text{m}$ and $1.19 \mu\text{m}$, respectively, and worn rates of $9.88 \times 10^{-6} \text{mm}^3/(\text{N} \times \text{m})$ and $8.29 \times 10^{-6} \text{mm}^3/(\text{N} \times \text{m})$. For both films, the wear scar depth exceeds the film thickness, which indicates that the films are completely worn through during the sliding process.

After annealing, the worn depth and worn rate of the HR_{N0} film show a significant reduction. The adhesion strength of the HR_{N0} film is slightly lower than that of the as-deposited film ($L_c = 39 \text{ N}$ (HR_{N0}) vs. $L_c = 61.3 \text{ N}$ (R_{N0})), which suggests that the wear resistance will be impaired. However, the XPS analysis results show that the HR_{N0} film has

a high MoO₃ solid lubricant content (30.6%) and a high H/E ratio (0.043), which collectively outweigh the effect of a lower adhesion strength and thus improve the wear resistance. Overall, the HR_{N43} film has the highest hardness (36.0 GPa), highest H/E ratio (0.072), and highest MoO₃ solid lubricant content (36.1%) of all the films after heat treatment. It thus shows the best wear performance. The poor resistance of the HR_{N50} and HR_{N56} films can be attributed to their low adhesion strengths ($L_c = 61.6$ N and 47.3 N) and H/E ratios (0.041, and 0.040). Among the annealed films, the HR_{N33} film exhibits the lowest adhesion strength ($L_c = 11.1$ N) and H/E ratio (0.034). It thus has the highest worn depth and worn rate among all the films.

Overall, the results presented in Table 6 show that the R_{N43} and HR_{N43} films have the highest hardness (33.0 and 36.0 GPa), highest H/E ratio (0.066 and 0.072), and highest MoO₃ solid lubrication content (48.2% and 36.1%, respectively). Thus, the two films show the best tribological properties among all the as-deposited and annealed films. Notably, the results also show that the tribological properties of the two films outperform those of the bare WC and HWC substrates, thus demonstrating their potential for protective films in machining and other applications.

3.5.3. Wear Mechanism

The R_{N0} and R_{N33} films were completely worn through during sliding, with wear scars deeply penetrating the substrate, indicating a similar wear mechanism. In contrast, the R_{N43}, R_{N50}, and R_{N56} films demonstrated improved wear resistance with similar mechanisms. Likewise, the HR_{N33}, HR_{N50}, and HR_{N56} films wore through to the substrate, exhibiting similar wear mechanisms. Notably, the R_{N43} and HR_{N43} films showed the highest wear resistance within their groups. Therefore, this section focuses exclusively on the wear surfaces and mechanisms of the R_{N0}, R_{N43}, HR_{N0}, and HR_{N43} films for simplicity.

Figure 10 presents SEM graphics and the corresponding EDS analysis results for the wear tracks on the R_{N0} and R_{N43} films. As shown in Area A of Figure 10a, the worn surface of the R_{N0} film is very rough. According to the EDS results, Area A has an oxygen content of 20.6 at.%, a C content of 22.6 at.%, and a N content of 5.7 at.%. The presence of these elements suggests that the rough surface is the result of adhesive wear, which leads to the transfer of material (nitrogen) from the Si₃N₄ ball and the adhesion of wear fragments on the surface. The high oxygen content also suggests the occurrence of moderate oxidation wear. Area B of the wear track (the white smooth area) has a high C content (69.4 at.%) and W content (16.3 at.%). Moreover, it contains only a minimal amount of the originally existed film elements. In other words, the EDS results confirm that the wear process causes the film to be removed and the wear scar to penetrate the underlying substrate. In general, the main wear mechanisms of the R_{N0} film are moderate oxidation wear and adhesive wear. The entire film fails during sliding as a result of adhesive wear, leading to the high and oscillating COF curve illustrated in Figure 10a. Overall, the results confirm that the R_{N0} film exhibits inferior tribological properties due to its low critical load ($L_c = 61.3$ N), low hardness (17.4 GPa), and low H/E ratio (0.028).

Figure 10b,c show the worn surface of the R_{N43} film. The wear trace is flatter and narrower than the trace on the R_{N0} film (528 μm vs. 803 μm). The enlarged image (see Figure 10c) shows the presence of grooves, most probably caused by hard worn debris during the wear test. The elemental composition of Area C in the central region of the wear track is almost identical to that of the originally existed film. However, the oxygen content is slightly higher (7.3 at.% vs. 5.2 at.%). Area D consists of black sheet debris with a high O content of 19.2 at.%, which suggests the occurrence of slight oxidation during the wear process.

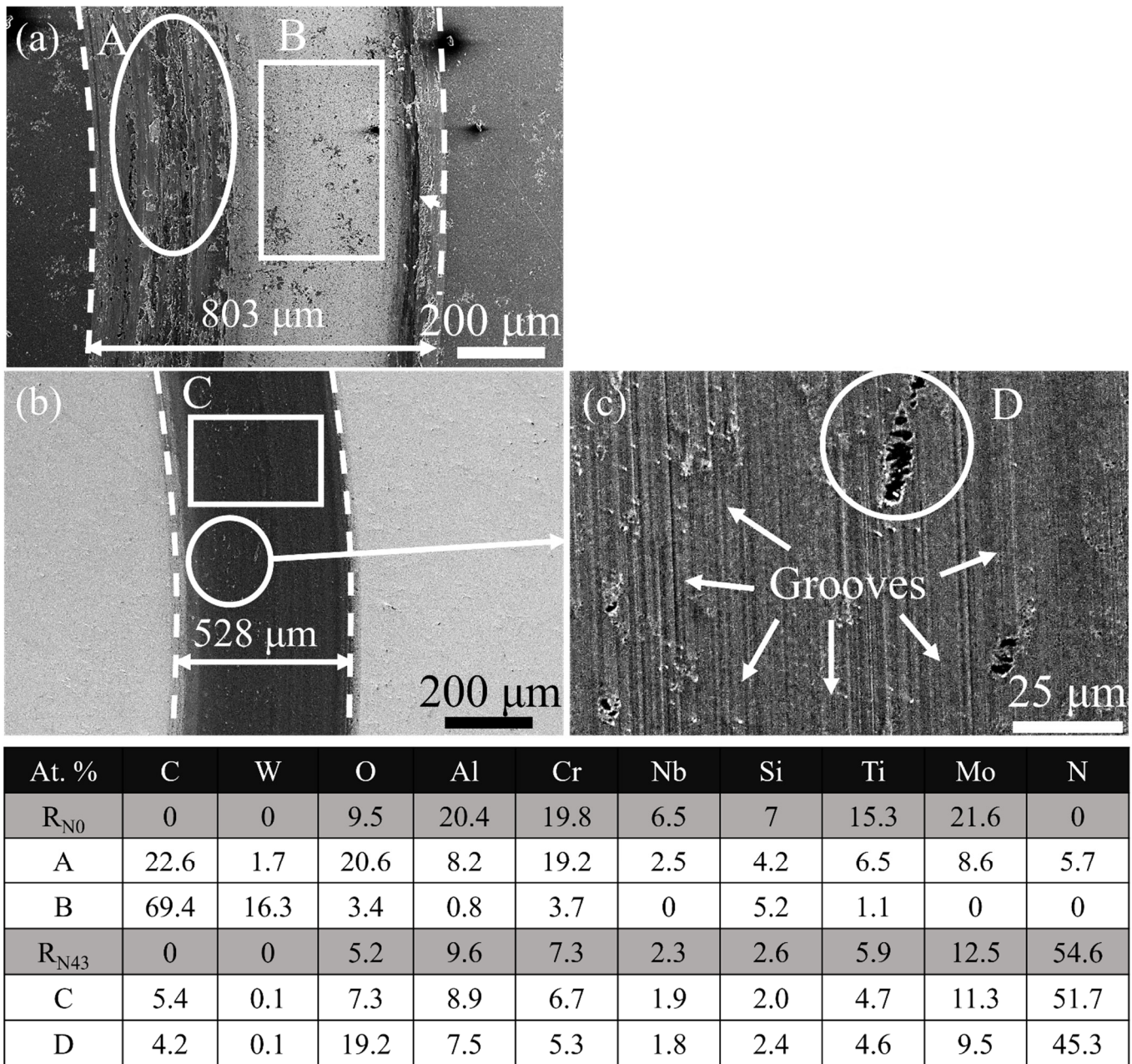


Figure 10. SEM graphics and EDS results of worn traces on (a) R_{N0} and (b) R_{N43} films and (c) R_{N43} film enlarged image and (Note: For comparative analysis, the originally existed elemental compositions of the R_{N0} , R_{N43} films are also shown).

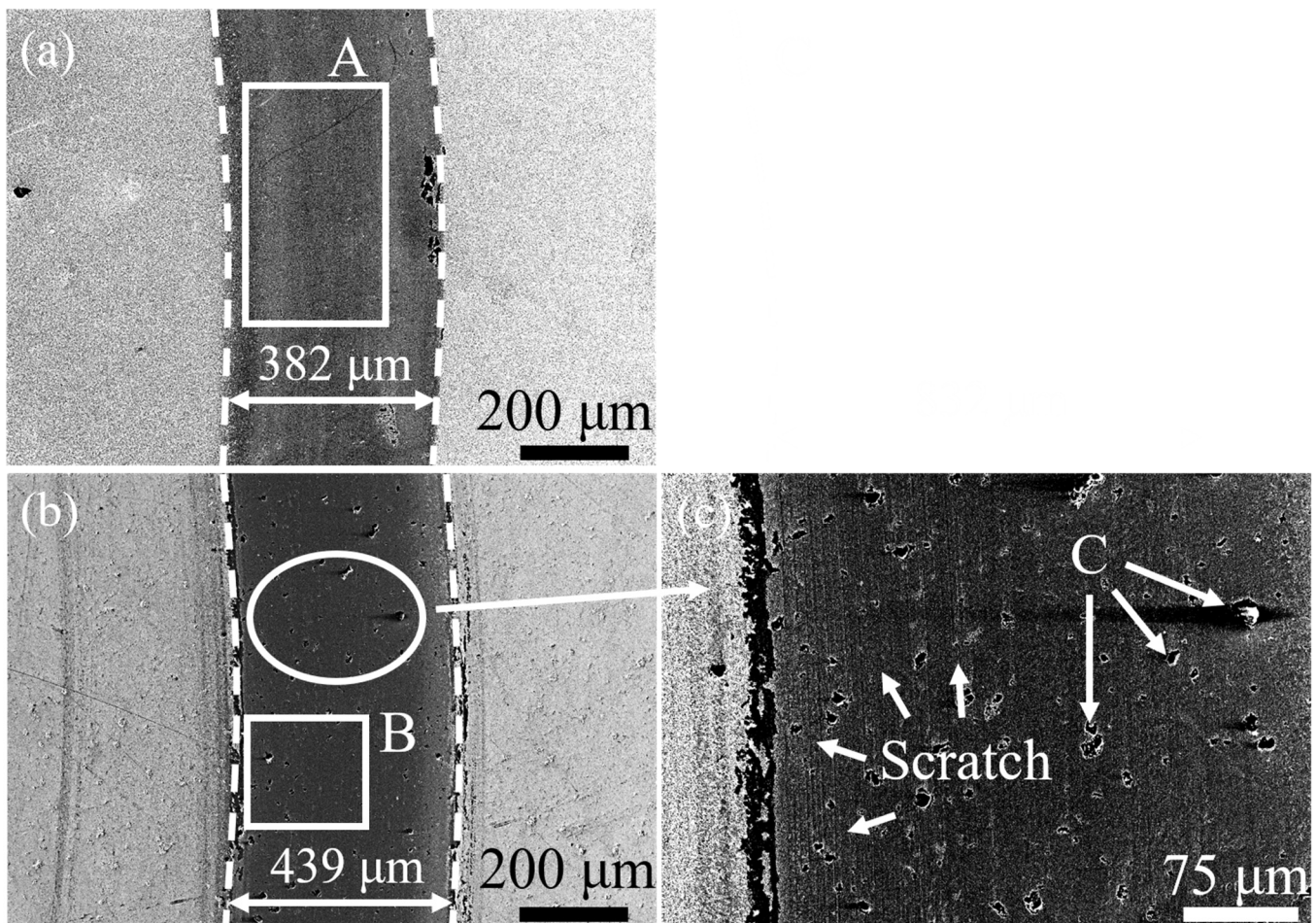
Both regions of the wear track contain a small amount of C (4.2–5.4 at.%) and W (0.1 at.%). However, the worn depth of the R_{N43} film (0.15 μm) is significantly lower than its total thickness (1.59 μm), which indicates that the film is not removed from the substrate during the sliding process. Thus, the low quantities of C and W identified in the wear track are most likely due to the detection depth range of the EDS system (0.5–3 μm), which causes the measurement process to detect elements in the WC substrate immediately beneath the wear track. In general, the SEM and EDS results suggest that the main wear mechanisms of the R_{N43} film are slight abrasive wear and slight oxidation. The morphologies of the abrasive particles and grooves are similar to those observed in [53]. The excellent wear performance of the film originates from its high hardness (33.0 GPa), high adhesion strength

(>100 N), high H/E ratio (0.066), and elevated MoO₃ solid lubricant content (48.2%), which lead to a low and stable COF curve, as shown in Figure 9a.

Figure 11a shows that the worn surface of the heat-treated HR_{N0} film is flatter than that of the as-deposited R_{N0} film. Moreover, the width of the wear track is reduced (382 μm vs. 803 μm). Most of the original film elements (Al, Cr, Nb, Si, Ti, and Mo) remain in the wear track. In addition, a small amount (7.4 at.%) of nitrogen transfer occurs from the Si₃N₄ counterbody. Notably, small quantities of C and W are detected in Area A (C: 6.3 at.% and W: 5.1 at.%). Since the HR_{N0} film does not wear through to the substrate during the sliding process, the C and W elements are again inferred to be the result of the EDS detection depth (3 μm) exceeding the HR_{N0} film thickness (2.33 μm). In general, the results suggest that the primary wear mechanism of the HR_{N0} film involves only slight material transfer from the Si₃N₄ ball. The HR_{N0} film produces a large quantity of 30.6% MoO₃, which acts as a solid lubricant. Consequently, the COF curve of the HR_{N0} film shown in Figure 9b has a lower and more stable value than that of the R_{N0} film. The enhanced wear performance of the HR_{N0} film is due to its increased hardness (20.0 GPa vs. 17.4 GPa) and higher H/E ratio (0.043 vs. 0.028).

Figure 11b,c show the worn surface of the HR_{N43} film. The worn width (439 μm) is smaller than that of the R_{N43} film (528 μm). In addition, the worn surface is noticeably smoother and exhibits only minor scratches. The EDS analysis results indicate that the elemental composition of Area B is nearly identical to that of the original film (Al, Si, Ti, Cr, Nb, Mo, and N). However, a slight increase in the O content is observed (14.6 at.% vs. 8.9 at.%), and small quantities of C (0.4 at.%) and W (0.1 at.%) are also detected. The wear track also contains some worn debris with a high oxygen content. For example, in Area C, the O content reaches as much as 65.2 at.%. Since the worn depth is only 0.1 μm and the HR_{N43} film has a thickness of 1.46 μm, the small amounts of C and W in Area C are again assumed to derive from the underlying substrate. In general, the results reveal that the wear mechanism of the HR_{N43} film is mainly slight oxidative wear, accompanied by slight abrasive wear and oxide formation. The morphologies of the abrasive particles and scratches are similar to those observed in [53]. Among the various films, the HR_{N43} film exhibits the best wear performance because of its highest hardness (36.0 GPa), highest H/E ratio (0.072), excellent adhesion strength (>100 N), and highest MoO₃ solid lubricant content (36.1%). Thus, the COF of the HR_{N43} film has a low and stable value, as shown in Figure 9b.

Collectively, the results presented in this section show that the R_{N43} and HR_{N43} films have the best tribological properties among all the deposited and annealed films, respectively. Specifically, they have the lowest worn depths (0.15 μm and 0.10 μm) and worn rates (0.49×10^{-6} mm³/Nm and 0.48×10^{-6} mm³/Nm), which are lower than the worn depths (0.23 μm and 0.25 μm) and worn rates (0.96×10^{-6} mm³/Nm and 1.02×10^{-6} mm³/Nm) of the WC and HWC substrates. The R_{N43} film exhibited a significant reduction in worn depth (34.8%) and worn rate (49.0%) compared with the WC substrate. Similarly, the HR_{N43} film demonstrated a marked improvement in the worn depth (60.0%) and worn rate (57.9%) relative to the HWC substrate. After high temperature annealing at 950 °C, the hardness of the HR_{N43} film increases from 33.0 to 36.0 GPa, and the H/E ratio increases from 0.066 to 0.072. Furthermore, the superior adhesion strength (>100 N) of the original R_{N43} film is retained, indicating that the HR_{N43} film has excellent thermal stability.



At. %	C	W	O	Al	Cr	Nb	Si	Ti	Mo	N
HR _{N0}	0	0	54.3	20.3	6.5	2.2	3.2	4.2	9.3	0
A	6.3	5.1	33.9	18.8	7.3	2.5	2.2	6.0	10.5	7.4
HR _{N43}	0	0	8.9	9.8	7.2	2.4	2.6	5.8	13.1	50.3
B	0.4	0.1	14.6	9.3	6.7	1.8	2.1	5.2	12.1	47.5
C	3.9	0.2	65.2	2.6	1.2	0.5	12.4	2.4	3.9	7.9

Figure 11. SEM graphics and EDS results for worn traces on (a) HR_{N0} film, (b) HR_{N43} film (regular magnification), and (c) HR_{N43} film (high magnification). (Note: For comparative analysis, the originally existed elemental compositions of the HR_{N0} and HR_{N43} films are also provided).

3.6. Machining Performance

Czan et al. [54] reported that the maximum temperature generated in the machining of nickel alloy Inconel 718 is around 950 °C. The results presented in Section 3.5 have shown that the HR_{N43} film exhibits excellent mechanical and tribological properties after annealing at 950 °C for 1 h and has superior thermal stability. Thus, the R_{N43} film was chosen for deposition on WC milling tools to perform cutting experiments using Inconel 718 workpieces. In order to compare, milling tests were also performed using a bare tool and an R_{N43}-coated tool.

Figure 12a,b present OM micrographs showing the notch wear and flank wear on the R_{N43}-coated tool and bare tool after completing a total cutting distance of 18 m. As shown

in Figure 12b, the flank wear on the bare tool is more severe than that on the R_{N43} -coated tool. The notch wear length on the R_{N43} -coated tool (550.6 μm) is considerably lesser than that of the bare tool (1209.4 μm). Thus, the results verify that the R_{N43} film yields an effective improvement in the wear resistance.

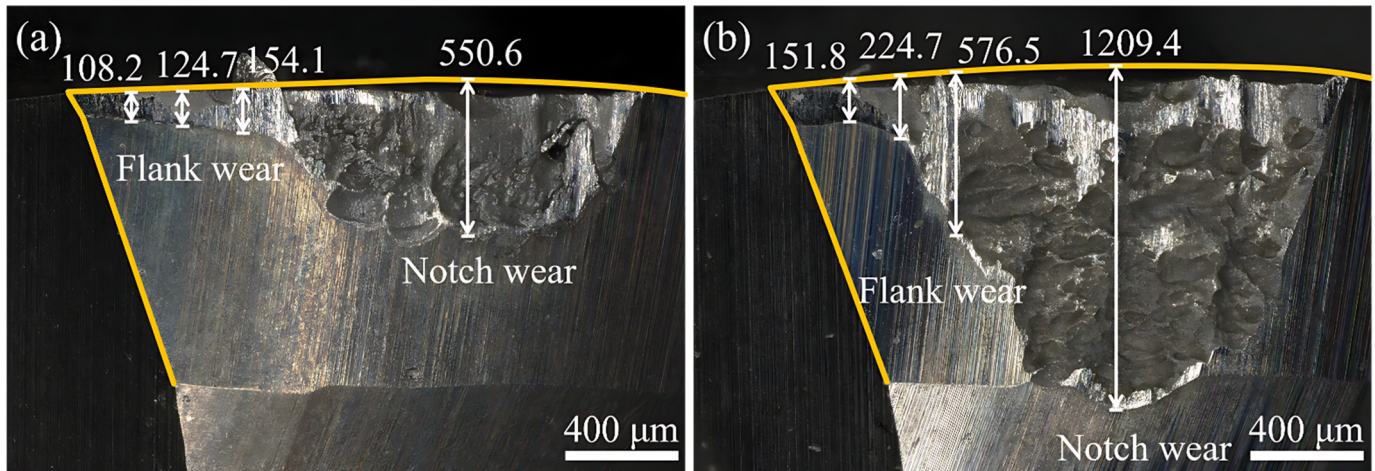


Figure 12. OM graphics showing the flank wear and notch wear on (a) bare WC cutting tool and (b) R_{N43} coated WC cutting tool completing a total processing distance of 18 m.

Figure 13a,b illustrate the average notch lengths and flank wears on the bare tool, R_{N43} -coated tool, and several other coated tools [23,26], after completing a total processing distance of 6, 12, and 18 m. The flank wear on the bare tool is 99.2 μm , 218.9 μm , and 358.0 μm after 6, 12, and 18 m, individually. The flank wear measurements show a large standard deviation due to the severity of the flank wear condition, as shown in Figure 12b. The flank wears of the R_{N43} -coated tool after the same milling distances are 87.1 μm , 117.6 μm , and 132.4 μm , respectively. Thus, compared with the bare tool, the R_{N43} film decreases the flank wear by 12.2%, 46.3%, and 63.0% completing a total processing distance of 6, 12, and 18 m, individually. The performance improvement offered by the coated tool increases with an increasing cutting distance owing to its excellent high-temperature thermal stability, high hardness, high adhesion strength, and superior wear resistance. As shown in Figure 13b, the notch wear lengths on the bare tool after completing a total processing distance of 6, 12, and 18 m are 708.9 μm , 1135.6 μm , and 1194.8 μm , respectively. In comparison, the notch wear lengths on the R_{N43} -coated tool are 172.3 μm , 388.6 μm , and 633.8 μm . Namely, the R_{N43} film decreases the notch wear by 72.8%, 65.8%, and 47.0% after completing a total processing distance of 6, 12, and 18 m, individually.

To demonstrate the superior wear resistance of the film in nickel-based alloy cutting tasks, Figure 13a,b also compare the wear of the coated tool with that of three other six-element HEA-coated tools presented in the literature, namely AlCrNbSiTi-N0, AlCrNbSiTi-N15, and AlCrNbSiTiVZr-N20 [23,26], under identical cutting conditions. After 18 m of cutting, the flank wear of the AlCrNbSiTi-N0 tool is 160.4 μm , while that of the AlCrNbSiTi-N15 tool is 154.4 μm , and that of the AlCrNbSiTiVZr-N20 tool is 151.6 μm . The R_{N43} -coated tool exhibits the lowest flank wear among the four films. In addition, its notch wear (633.8 μm) is also lower than that of the AlCrNbSiTiVZr-N20 film (1071.6 μm). In other words, in addition to its superior flank wear, the R_{N43} film also shows a lower notch wear, indicating an improved resistance to cutting heat accumulation and chip flow. Overall, the results in Figure 13 demonstrate that the R_{N43} film significantly enhances the wear performance of the tool and is thus expected to result in an extended service life.

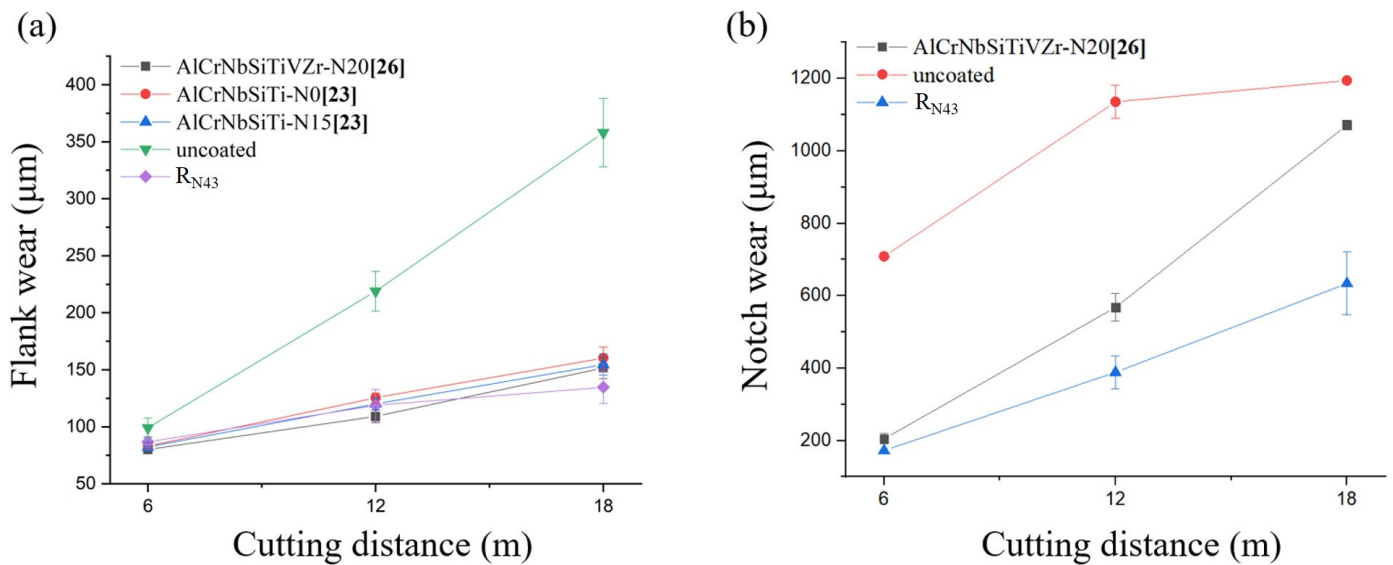


Figure 13. (a) Flank wear and (b) Notch wear of bare WC cutting tool and R_{N43} coated WC cutting tool compared with other coated tools after completing three processing distances of 6, 12, and 18 m, individually.

4. Conclusions

(AlCrNbSiTiMo)N HEA films were deposited on WC substrates using a radio-frequency magnetron sputtering system with single multiple-element powder hot-pressed sintered AlCrNbSiTi targets and a single vacuum-arc-melting Mo target. Sputtering was performed at various nitrogen flow rates. The film with the optimal tribological properties was deposited on WC cutting tools and used in machining trials using Inconel 718 workpieces. The results of the experiments can be outlined as follows.

- (1) As the N₂ flow rate increased, the R_{N43} film reached a nitrogen saturation condition of 54.6 at.%. The high nitrogen content resulted in the formation of strong nitride bonds, giving the film excellent thermal stability. After annealing, all the films exhibited a denser structure.
- (2) The hardness of the films initially increased with an increasing nitrogen content due to the solid-solution strengthening effect and the subsequent formation of Me-N bonds. The hardness of the as-deposited R_{N43} film reached 33.0 GPa. For the annealed films, the film structures were denser, and the bonding strength between the film elements and nitrogen was enhanced. Consequently, the hardness of all the films increased. The HR_{N43} film showed the highest hardness (36.0 GPa).
- (3) The HR_{N43} film had the highest hardness, H/E ratio, adhesion strength, and amount of MoO₃ solid lubricant. It thus showed the best tribological properties. Compared with the bare HWC substrate, the worn depth and worn rate of the HR_{N43} film were reduced by 60.0% and 57.9%, respectively.
- (4) Compared with the bare milling tool, the flank wear and notch wear of the R_{N43}-coated tool were reduced by 63.0% and 47.0%, respectively. Therefore, the R_{N43} film displays to be an appropriate film material for processing Inconel 718 alloy. In particular, the R_{N43} film provides an excellent machining performance and significantly extends the tool life, resulting in lower tool replacement costs during Inconel 718 processing in industry.

Author Contributions: Conceptualization, J.-H.H. and W.-H.K.; methodology, J.-H.H. and W.-H.K.; software, W.-C.L. and R.-H.C.; validation, W.-H.K., W.-C.L. and R.-H.C.; formal analysis, J.-H.H. and W.-H.K.; investigation, W.-H.K., W.-C.L. and R.-H.C.; resources, J.-H.H. and W.-H.K.; data curation, W.-H.K., W.-C.L. and R.-H.C.; writing—original draft preparation, W.-H.K., W.-C.L. and R.-H.C.;

writing—review and editing, J.-H.H. and W.-H.K.; visualization, W.-C.L. and R.-H.C.; supervision, J.-H.H. and W.-H.K. All authors have read and agreed to the published version of the manuscript.

Funding: We thank the National Science and Technology Council of Taiwan for financial support of this study under Contract No. NSTC 112-2221-E-270-001-MY2.

Data Availability Statement: The original contributions presented in the study are included in the article, further inquiries can be directed to the corresponding author.

Conflicts of Interest: The authors declare no conflicts of interest.

References

1. Cantor, B.; Kim, K.B.; Warren, P.J. Novel multicomponent amorphous alloys. *Mater. Sci. Forum.* **2002**, *386–388*, 27–32.
2. Yeh, J.W.; Chen, S.K.; Lin, S.J.; Gan, J.Y.; Chin, T.S.; Shun, T.T.; Tsau, C.H.; Chang, S.Y. Nanostructured high-entropy alloys with multiple principal elements: Novel alloy design concepts and outcomes. *Adv. Eng. Mater.* **2004**, *6*, 299–303. [[CrossRef](#)]
3. Huang, P.K.; Yeh, J.W. Effects of substrate temperature and post-annealing on microstructure and properties of (AlCrNbSiTiV)N coatings. *Thin Solid Films* **2009**, *518*, 180–184. [[CrossRef](#)]
4. Lai, C.H.; Cheng, K.H.; Lin, S.J.; Yeh, J.W. Mechanical and tribological properties of multi-element (AlCrTaTiZr)N coatings. *Surf. Coat. Technol.* **2008**, *202*, 3732–3738. [[CrossRef](#)]
5. Lo, W.L.; Hsu, S.Y.; Lin, Y.C.; Tsai, S.Y.; Lai, Y.T.; Duh, J.G. Improvement of high entropy alloy nitride coatings (AlCrNbSiTiMo)N on mechanical and high temperature tribological properties by tuning substrate bias. *Surf. Coat. Technol.* **2020**, *401*, 126247. [[CrossRef](#)]
6. Zhao, Y.; Chen, S.; Chen, Y.; Wu, S.; Xie, W.; Yan, W.; Wang, S.; Liao, B.; Zhang, S. Super-hard and anti-corrosion (AlCrMoSiTi)N_x high entropy nitride coatings by multi-arc cathodic vacuum magnetic filtration deposition. *Vacuum* **2022**, *195*, 110685. [[CrossRef](#)]
7. Feng, X.; Zhang, K.; Zheng, Y.; Zhou, H.; Wan, Z. Chemical state, structure and mechanical properties of multi-element (CrTaNbMoV)N_x films by reactive magnetron sputtering. *Mater. Chem. Phys.* **2020**, *239*, 121991. [[CrossRef](#)]
8. Chang, H.W.; Huang, P.K.; Yeh, J.W.; Davison, A.; Tsau, C.H.; Yang, C.C. Influence of substrate bias, deposition temperature and post-deposition annealing on the structure and properties of multi-principal-component (AlCrMoSiTi)N coatings. *Surf. Coat. Technol.* **2008**, *202*, 3360–3366. [[CrossRef](#)]
9. Lin, Y.C.; Hsu, S.Y.; Song, R.W.; Lo, W.L.; Lai, Y.T.; Tsai, S.Y.; Duh, J.G. Improving the hardness of high entropy nitride (Cr_{0.35}Al_{0.25}Nb_{0.12}Si_{0.08}V_{0.20})N coatings via tuning substrate temperature and bias for anti-wear applications. *Surf. Coat. Technol.* **2020**, *403*, 126417. [[CrossRef](#)]
10. Chang, C.H.; Yang, C.B.; Sung, C.C.; Hsu, C.Y. Structure and tribological behavior of (AlCrNbSiTiV)N film deposited using direct current magnetron sputtering and high power impulse magnetron sputtering. *Thin Solid Films* **2018**, *668*, 63–68. [[CrossRef](#)]
11. Shen, W.; Tsai, M.; Tsai, K.; Juan, C.; Tsai, C.; Yeh, J.; Chang, Y. Superior oxidation resistance of (Al_{0.34}Cr_{0.22}Nb_{0.11}Si_{0.11}Ti_{0.22})₅₀N₅₀ high-entropy nitride. *J. Electrochem. Soc.* **2013**, *160*, C531. [[CrossRef](#)]
12. Wang, D.Y.; Chang, C.L.; Ho, W.Y. Oxidation behavior of diamond-like carbon films. *Surf. Coat. Technol.* **1999**, *120*, 138–144. [[CrossRef](#)]
13. El-Wardany, T.I.; Mohammed, E.; Elbestawi, M.A. Cutting temperature of ceramic tools in high speed machining of difficult-to-cut materials. *Int. J. Mach. Tools Manuf.* **1996**, *36*, 611–634. [[CrossRef](#)]
14. Döleker, K.M.; Özgürlük, Y.; Gokcekaya, O.; Günen, A.; Erdoğan, A. High-temperature corrosion and oxidation properties of borided CoCrFeNiAl_{0.5}Nb_{0.5} HEA. *Surf. Coat. Technol.* **2023**, *470*, 129856. [[CrossRef](#)]
15. Kuzminova, Y.O.; Firsov, D.G.; Shibalova, A.A.; Evlashin, S.A.; Shishkovsky, I.V.; Dautov, S.S. The oxidation behavior of the CrFeCoNiAl_x (x = 0, 1.0, and 5.0 wt%) high-entropy alloy synthesized with Al elemental powder via powder bed fusion technique at high temperatures. *Micron* **2023**, *166*, 103399. [[CrossRef](#)]
16. Hong, Y.; Kivy, M.B.; Zaem, M.A. Competition between formation of Al₂O₃ and Cr₂O₃ in oxidation of Al_{0.3}CoCrCuFeNi high entropy alloy: A first-principles study. *Scr. Mater.* **2019**, *168*, 139–143. [[CrossRef](#)]
17. Dong, J.; Long, X.J.; Zhou, L.J.; Deng, H.; Zhang, H.C.; Qiu, W.B.; Yin, M.; Yin, G.F.; Chen, L.Q. Effect of Ti addition on high-temperature properties of AlCoCrFeNi_{2.1} coating prepared on Ti-6Al-4V alloy. *Corros. Sci.* **2023**, *217*, 111105. [[CrossRef](#)]
18. Wang, M.; Zhan, L.J.; Peng, J. Nb micro-alloying on enhancing yield strength and hindering intermediate temperature decomposition of a carbon-doped high-entropy alloy. *J. Alloys Compd.* **2023**, *940*, 168896. [[CrossRef](#)]
19. Zhao, W.; Yu, K.; Ma, Q.; Song, C.; Xiao, G.; Zhang, H.; Lv, Y.; Guo, N.; Li, Z. Synergistic effects of Mo and in-situ TiC on the microstructure and wear resistance of AlCoCrFeNi high entropy alloy fabricated by laser cladding. *Tribol. Int.* **2023**, *188*, 108827. [[CrossRef](#)]
20. Pei, X.; Du, Y.; Li, T.; Wang, H.; Hu, M.; Wang, H. A combinatorial evaluation of TiZrV_{0.5}Nb_{0.5}Si_x refractory high entropy alloys: Microstructure, mechanical properties, wear and oxidation behaviors. *Mater. Charact.* **2023**, *201*, 112956. [[CrossRef](#)]
21. Zhao, Y.; Feng, K.; Yao, C.; Li, Z. Effect of MoO₃ on the microstructure and tribological properties of laser-clad Ni60/nanoCu/h-BN/MoO₃ composite coatings over wide temperature range. *Surf. Coat. Technol.* **2020**, *387*, 125477. [[CrossRef](#)]

22. Zin, V.; Montagner, F.; Miorin, E.; Mortalò, C.; Tinazzi, R.; Bolelli, G.; Lusvarghi, L.; Togni, A.; Frabboni, S.; Gazzadi, G.; et al. Effect of Mo content on the microstructure and mechanical properties of CoCrFeNiMo_x HEA coatings deposited by high power impulse magnetron sputtering. *Surf. Coat. Technol.* **2024**, *476*, 130244. [[CrossRef](#)]
23. Kao, W.H.; Su, Y.L.; Horng, J.H.; Wu, W.C. Mechanical, tribological and anti-corrosion properties of AlCrNbSiTi high entropy coatings with various nitrogen fluxes and application to nickel-based alloy milling. *Mater. Chem. Phys.* **2022**, *282*, 125999. [[CrossRef](#)]
24. Zhang, X.; Pelenovich, V.; Zeng, X.; Wan, Q.; Liu, J.; Pogrebnyak, A.; Guo, Y.; Liu, Y.; Lei, Y.; Yang, B. Unravel hardening mechanism of AlCrNbSiTi high-entropy alloy coatings. *J. Alloys Compd.* **2023**, *965*, 171222. [[CrossRef](#)]
25. Shen, W.J.; Tsai, M.H.; Chang, Y.S.; Yeh, J.W. Effects of substrate bias on the structure and mechanical properties of (Al_{1.5}CrNb_{0.5}Si_{0.5}Ti)_{N_x} coatings. *Thin Solid Films* **2012**, *520*, 6183–6188. [[CrossRef](#)]
26. Kao, W.H.; Su, Y.L.; Horng, J.H.; Cheng, Y.T. Mechanical behavior, tribological properties, and thermal stability of (AlCrNbSi-TiVZr)N high entropy alloy nitride coatings and their application to Inconel 718 milling. *Mater. Chem. Phys.* **2024**, *314*, 128816. [[CrossRef](#)]
27. Peng, C.; Zhong, L.; Gao, L.; Li, L.; Nie, L.; Wu, A.; Huang, R.; Tian, W.; Yin, W.; Wang, H.; et al. Implementation of near-infrared spectroscopy and convolutional neural networks for predicting particle size distribution in fluidized bed granulation. *Int. J. Pharm.* **2024**, *655*, 124001. [[CrossRef](#)]
28. Ren, B.; Yan, S.Q.; Zhao, R.F.; Liu, Z.X. Structure and properties of (AlCrMoNiTi)_{N_x} and (AlCrMoZrTi)_{N_x} films by reactive RF sputtering. *Surf. Coat. Technol.* **2013**, *235*, 764–772. [[CrossRef](#)]
29. Liang, S.C.; Tsai, D.C.; Chang, Z.C.; Sung, H.S.; Lin, Y.C.; Yeh, Y.J.; Deng, M.J.; Shieu, F.S. Structural and mechanical properties of multi-element (TiVCrZrHf)N coatings by reactive magnetron sputtering. *Appl. Surf. Sci.* **2011**, *258*, 399–403. [[CrossRef](#)]
30. ASTM G99-17; Standard Test Method for Wear Testing with a Pin-on-Disk Apparatus. ASTM: West Conshohocken, PA, USA, 2023.
31. Cui, P.; Li, W.; Liu, P.; Zhang, K.; Ma, F.; Chen, X.; Feng, R.; Liaw, P.K. Effects of nitrogen content on microstructures and mechanical properties of (AlCrTiZrHf)N high-entropy alloy nitride films. *J. Alloys Compd.* **2020**, *834*, 155063. [[CrossRef](#)]
32. Farhadizadeh, A.; Vlček, J.; Houška, J.; Haviar, S.; Čerstvý, R.; Červená, M.; Zeman, P.; Matas, M. Effect of nitrogen content on high-temperature stability of hard and optically transparent amorphous Hf-Y-Si-BCN coatings. *Ceram. Int.* **2023**, *49*, 6086–6093. [[CrossRef](#)]
33. Chang, S.Y.; Lin, S.Y.; Huang, Y.C.; Wu, C.L. Mechanical properties, deformation behaviors and interface adhesion of (AlCrTaTiZr)_{N_x} multi-component coatings. *Surf. Coat. Technol.* **2010**, *204*, 3307–3314. [[CrossRef](#)]
34. Hsueh, H.T.; Shen, W.J.; Tsai, M.H.; Yeh, J.W. Effect of nitrogen content and substrate bias on mechanical and corrosion properties of high-entropy films (AlCrSiTiZr)_{100-x}N_x. *Surf. Coat. Technol.* **2012**, *206*, 4106–4112. [[CrossRef](#)]
35. Zhao, Y.; Jiang, M.; Xu, J.; Xie, Z.H.; Munroe, P. Effects of nitrogen concentration on the microstructure and mechanical properties of nanocrystalline (TiZrNbTaMo) N high-entropy nitride coatings: Experimental investigations and first-principles calculations. *Vacuum* **2024**, *219*, 112715. [[CrossRef](#)]
36. Peng, X.; Chen, L. Effect of high entropy alloys TiVCrZrHf barrier layer on microstructure and texture of Cu thin films. *Mater. Lett.* **2018**, *230*, 5–8. [[CrossRef](#)]
37. You, D.; Jiang, Y.; Li, W.; Zhao, Y.; Wan, L.; Tan, M. Annealing-induced defects and optical degradation in sputter-deposited silicon nitride: Implications for photonic applications. *Ceram. Int.* **2024**, *50*, 22553–22564. [[CrossRef](#)]
38. Tsai, D.C.; Chang, Z.C.; Kuo, B.H.; Shiao, M.H.; Chang, S.Y.; Shieu, F.S. Structural morphology and characterization of (AlCrMo-TaTi)N coating deposited via magnetron sputtering. *Appl. Surf. Sci.* **2013**, *282*, 789–797. [[CrossRef](#)]
39. Ougier, M.; Michau, A.; Lomello, F.; Schuster, F.; Maskrot, H.; Schlegel, M.L. High-temperature oxidation behavior of HiPIMS as-deposited Cr-Al-C and annealed Cr₂AlC coatings on Zr-based alloy. *J. Nucl. Mater.* **2020**, *528*, 151855. [[CrossRef](#)]
40. Liang, S.C.; Chang, Z.C.; Tsai, D.C.; Lin, Y.C.; Sung, H.S.; Deng, M.J.; Shieu, F.S. Effects of substrate temperature on the structure and mechanical properties of (TiVCrZrHf)N coatings. *Appl. Surf. Sci.* **2011**, *257*, 7709–7713. [[CrossRef](#)]
41. Cheng, K.H.; Lai, C.H.; Lin, S.J.; Yeh, J.W. Structural and mechanical properties of multi-element (AlCrMoTaTiZr)_{N_x} coatings by reactive magnetron sputtering. *Thin Solid Films* **2011**, *519*, 3185–3190. [[CrossRef](#)]
42. Tien, S.K.; Lin, C.H.; Tsai, Y.Z.; Duh, J.G. Effect of nitrogen flow on the properties of quaternary CrAlSiN coatings at elevated temperatures. *Surf. Coat. Technol.* **2007**, *202*, 735–739. [[CrossRef](#)]
43. Hu, J.; Wang, J.; Wei, Y.; Wu, Q.; Zhang, F.; Xu, Q. Effect of film growth thickness on the refractive index and crystallization of HfO₂ film. *Ceram. Int.* **2021**, *47*, 33751–33757. [[CrossRef](#)]
44. Ma, D.L.; Deng, Q.Y.; Liu, H.Y.; Li, Y.T.; Leng, Y.X. Microstructure and properties of Ti₂AlN thin film synthesized by vacuum annealing of high power pulsed magnetron sputtering deposited Ti/AlN multilayers. *Surf. Coat. Technol.* **2021**, *425*, 127749. [[CrossRef](#)]
45. Zhang, F.; Ma, H.; Zhao, R.; Yu, G.; Chen, J.; Yin, F. Microstructure, mechanical and corrosion performance of magnetron sputtered (Al_{0.5}CoCrFeNi)_{N_x} high-entropy alloy nitride films. *J. Alloys Compd.* **2023**, *968*, 172158. [[CrossRef](#)]
46. Ren, B.; Shen, Z.; Liu, Z. Structure and mechanical properties of multi-element (AlCrMnMoNiZr)_{N_x} coatings by reactive magnetron sputtering. *J. Alloys Compd.* **2013**, *560*, 171–176. [[CrossRef](#)]
47. Othman, M.; Bushroa, A.R. Evaluation techniques and improvements of adhesion strength for TiN coating in tool applications: A review. *J. Adhes. Sci. Technol.* **2015**, *29*, 569–591. [[CrossRef](#)]

48. Abuzaid, W.Z.; Sangid, M.D.; Carroll, J.D.; Sehitoglu, H.; Lambros, J. Slip transfer and plastic strain accumulation across grain boundaries in Hastelloy X. *J. Mech. Phys. Solid.* **2012**, *60*, 1201–1220. [[CrossRef](#)]
49. Pang, X.; Yang, H.; Liu, X.; Gao, K.; Wang, Y.; Volinsky, A.A.; Levin, A.A. Annealing effects on microstructure and mechanical properties of sputtered multilayer $\text{Cr}_{(1-x)}\text{Al}_x\text{N}$ films. *Thin Solid Films* **2011**, *519*, 5831–5837. [[CrossRef](#)]
50. Leyland, A.; Matthews, A. On the significance of the H/E ratio in wear control: A nanocomposite coating approach to optimized tribological behaviour. *Wear* **2000**, *246*, 1–11. [[CrossRef](#)]
51. Chang, C.L.; Lee, J.W.; Tseng, M.D. Microstructure, corrosion and tribological behaviors of TiAlSiN coatings deposited by cathodic arc plasma deposition. *Thin Solid Films* **2009**, *517*, 5231–5236. [[CrossRef](#)]
52. Zhou, Q.; Huang, B.; Zhang, E.G.; Peng, Z.Y.; Chen, Q.; Liang, D.D. Improving the mechanical and tribological properties of TiAlSiN coatings by annealing. *Vacuum* **2023**, *214*, 112249. [[CrossRef](#)]
53. Jamali, A.; Mirsalehi, S.E. Production of AA7075/ZrO₂ nanocomposite using friction stir processing: Metallurgical structure, mechanical properties and wear behavior. *CIRP J. Manuf. Sci. Technol.* **2022**, *37*, 55–69. [[CrossRef](#)]
54. Czan, A.; Sajgalik, M.; Holubjak, J.; Zauskova, L.; Czanova, T.; Martikan, P. Identification of temperatures in cutting zone when dry machining of nickel alloy Inconel 718. *Procedia Manuf.* **2017**, *14*, 66–75. [[CrossRef](#)]

Disclaimer/Publisher’s Note: The statements, opinions and data contained in all publications are solely those of the individual author(s) and contributor(s) and not of MDPI and/or the editor(s). MDPI and/or the editor(s) disclaim responsibility for any injury to people or property resulting from any ideas, methods, instructions or products referred to in the content.